



Constraints on dust aerosols from the Mars Exploration Rovers using MGS overflights and Mini-TES

M. J. Wolff,¹ M. D. Smith,² R. T. Clancy,¹ N. Spanovich,³ B. A. Whitney,¹
 M. T. Lemmon,⁴ J. L. Bandfield,⁵ D. Banfield,⁶ A. Ghosh,⁷ G. Landis,⁸
 P. R. Christensen,⁵ J. F. Bell III,⁶ and S. W. Squyres⁶

Received 2 July 2006; revised 3 September 2006; accepted 15 November 2006; published 30 December 2006.

[1] Overflights of the Mars Exploration Rovers (MER) by the Mars Global Surveyor (MGS) provide a unique opportunity to examine some of the basic properties of dust aerosols, starting with one of the most fundamental, the indices of refraction ($m = n + ik$) in the infrared. The upward-viewing geometry of the Miniature Thermal Emission Spectrometer (Mini-TES) and the combined contemporaneous observations from both MER and MGS are powerful tools. Their use allows atmospheric retrievals to directly determine n and k while offering constraints for the menagerie of other radiative transfer input parameters. We exploit these coordinated observing campaigns, along additional data sources, to carry out series of radiative transfer analyses that ultimately return the set of refractive indices. We apply the resulting m to a larger sample of Mini-TES data to both further validate our approach and retrieve several other aerosol properties, including dust optical depth, dust size, and a measure of the vertical mixing profile. We find good agreement with the empirical approach of Smith et al. (2006), in terms of both the optical depths themselves and the frequency dependence of their extinction cross section and single scattering albedo. The retrieved dust sizes vary from near $1.3 \mu\text{m}$ to $1.8 \mu\text{m}$ within the selected sample, with a precision estimated to be $\simeq 0.1\text{--}0.2 \mu\text{m}$. The vertical mixing profile evolves from well-mixed to appreciably confined by $L_S \sim 30^\circ$. For Spirit (MER-A), there is an abrupt transition back to a more well-mixed vertical profile with the onset of regional dust activity at $L_S \sim 140^\circ$. We discuss the lack of a definitive detection of water ice clouds in Mini-TES observations and the potential effects of vertical gradients in particle size distribution. Finally, as part of coordinated overflight analyses, an atmospherically corrected TES Lambert albedo map is derived and presented in Appendix A.

Citation: Wolff, M. J., et al. (2006), Constraints on dust aerosols from the Mars Exploration Rovers using MGS overflights and Mini-TES, *J. Geophys. Res.*, *111*, E12S17, doi:10.1029/2006JE002786.

1. Introduction

[2] For any studies of the Martian atmosphere involving the transport of optical and infrared (IR) radiation, the

radiative properties of aerosols represent a basic and necessary parameter set. While empirical approaches do exist, at least in the IR (e.g., factor analysis, spectral deconvolution, etc. [cf. Bandfield et al., 2000; Smith et al., 2000]), their use implicitly minimizes the amount of aerosol information that can be usefully derived. In contrast, analyses that start with the indices of refraction allow for direct access to particle microphysical properties such as size.

[3] Previous work with Viking, Pathfinder, and Mars Exploration Rover (MER) visible data has resulted in a reasonable degree of dust optical property characterization for the $0.4\text{--}1.0 \mu\text{m}$ wavelength range [Ockert-Bell et al., 1997; Tomasko et al., 1999; Lemmon et al., 2004]. Results for the infrared (IR) using (non-limb viewing) Mariner 9 and MGS data have provided useful groundwork in this area [e.g., Clancy et al., 1995; Snook, 1999; Snook et al., 2000; Hansen, 2003; Wolff and Clancy, 2003]. Despite the varying amounts of success in their original application, none of the indices produce satisfactory agreement with the MER IR

¹Space Science Institute, Boulder, Colorado, USA.

²Goddard Space Flight Center, Greenbelt, Maryland, USA.

³Jet Propulsion Laboratory, California Institute of Technology, Pasadena, California, USA.

⁴Department of Atmospheric Sciences, Texas A&M University, College Station, Texas, USA.

⁵Department of Geological Sciences, Arizona State University, Tempe, Arizona, USA.

⁶Department of Astronomy, Cornell University, Ithaca, New York, USA.

⁷Department of Earth and Planetary Sciences, University of Tennessee, Knoxville, Tennessee, USA.

⁸Photovoltaics and Space Environment Branch, NASA John Glenn Research Center, Cleveland, Ohio, USA.

observations without recourse to unphysical parameters (i.e., average sizes smaller than $1\ \mu\text{m}$). Previous IR analyses using orbital data sets would seem to have been limited by the dominance of the absorption component in non-limb viewing geometry.

[4] One can overcome the orbital limitation by exploiting the increased importance of scattering in the upward-viewing thermal IR geometry offered by MER. In principle, the use of limb observations could provide a similar emphasis on scattering processes. Such an analysis is significantly more complicated than that to be employed here. In addition, limb analyses would fold in additional radiative transfer model parameters and their associated uncertainties. However, what one seeks is actually a *reduction* of such issues. Ideally, one would like to use a data set that spans multiple observations that are dominated by dust aerosols with the same general physical characteristics, but which also contains complementary data that allow to constrain key parameters like the volume mixing ratio and the particle size (the atmospheric equivalent of “ground truth”).

[5] Remote sensing observations of the Martian atmosphere do not easily lend themselves to the notion of ground truth. While one might consider a high fidelity measurement from a surface platform (such as optical depth from direct solar imaging) to represent some degree of ground truth, connecting a series of orbital spacecraft observations to those of a surface station requires a temporal, as well as a spatial, overlap to account for the dynamical nature of the atmosphere. This concept of an “overflight” was exploited during the Viking era to provide a connection between lander and orbiter measurements of optical depth. Combined analyses have produced additional physical insights into Martian aerosols. *Hunt* [1979] and *Martin* [1986] examine Infrared Thermal Mapper observations obtained near the site with the context of lander data; *Clancy and Lee* [1991] employ the lander optical depths as a demonstration of the viability of their emission phase function retrieval methodology. However, the overflights of the Viking era remain fundamentally limited by two aspects: the absence of multi-instrument coordinated (i.e., simultaneous, or nearly so) observations, and the lack of similar instrument capabilities on both the surface and the orbital platforms.

[6] The MER sites experience two overflights per sol (one day, one night) by both the Mars Global Surveyor (MGS) and the Mars Odyssey (MO) spacecraft. Less often, but typically with a longer duration, Mars Express (MEX) provides similar opportunities. Given the frequency of such occasions, MER (and MGS) operational constraints (e.g., power and data resources) require that one discriminate among the various overpasses in the planning of coordinated observing campaigns. We selected overflights in which the rover was located with a few degrees of the spacecraft nadir. The majority of the events that ultimately were sequenced involves MGS, primarily due to number of overflights, the overlap of instrument sensitivity ranges, and the ability to obtain planning support from the relevant spacecraft planning teams. Several campaigns did occur also in conjunction with MEX [e.g., *Arvidson et al.*, 2004, 2005]. In addition, while an opportunity occurs with Mars Odyssey during every UHF communication session, to our knowledge, no coordinated efforts have been made to explicitly connect MER and MO observations during these periods. In

any case, we restrict our attention in this paper solely to the MGS overflights.

[7] The combination of MGS and MER instruments provides for leveraged atmospheric studies. That is to say, by combining the data from both platforms, one obtains a more complete picture than would be possible from analysis of each data set independently. More specifically, one can eliminate a large degree of potential uncertainty in the retrieved parameters by constructing thermal profiles from the surface (20 m) to more than 30 km using the $667\ \text{cm}^{-1}$ CO_2 band [*Smith et al.*, 2006], select the data with minimal amounts of water ice aerosols, and provide useful constraints on both the particle size distribution and the vertical mixing profile. With such a data set in hand, one can proceed with the derivation of the refractive indices. Subsequently, one may then move forward with more general aerosol retrievals (i.e., optical depth, particle size, vertical mixing profiles) from a sample of data that includes a wide-range of dust properties and conditions.

[8] We begin with a brief survey of the observations to be analyzed, including an assessment of the relevant errors and uncertainties. In section 3.1, we cover the radiative transfer algorithms employed and clarify several aspects of the input particle cross sections and surface properties. Next, we carry out sensitivity studies of several parameters that embody the unique aspect of the upward-viewing thermal IR geometry. The results from a set of coordinated overflight observations and the subsequent refractive index analyses are presented in section 5. We then apply our optical properties to two subsets of MER IR data, examining variations in dust loading, particle sizes, and, to a more qualitative degree, vertical mixing profiles. Finally, we discuss several aspects of our retrievals, including the problematic nature of water ice aerosol detections and the issue of vertical variations in particle sizes.

2. Observations and Instruments

[9] In terms of the actual coordinated MER-MGS overflights, we focus on those that occurred within the first four months of landed operations (sols 1–120). During this period, one finds a total of six such campaigns (see Table 1), each of which involves the same type of observations: nadir wide-angle imaging with the Mars Observer Camera (MOC) and an emission phase function (EPF) sequence with the Thermal Emission Spectrometer (TES). While MOC imagery can be extremely useful in studies of condensate clouds, its application to dust characterization can be problematic at low and moderate loading levels, particularly for near-nadir viewing geometry, by dint of the optically neutral nature of the dust with respect to moderate-to-bright surfaces. Given our focus on dust aerosols, we do not include any MOC data in the analyses presented here. Instead, in order to provide an optical counterpart to the MER data, we employ TES solarband bolometer data. In this case, the variation of the atmospheric pathlength throughout the observation avoids the atmosphere-surface contrast issue associated with the MOC data.

2.1. MER Observations

[10] The MER coordinated observations were designed to provide simultaneous IR sounding by the Miniature

Table 1. Coordinated Overflight Observation Summary

Sol ^a	LTST ^b	Elevation ^c	L_S	Comments ^d
22B	13:32	88.9°	350.4°	1
46A	13:36	89.1°	352.3°	1
68B	13:48	88.5°	13.9°	1
92A	13:52	88.5°	15.6°	1
115A	14:02	87.5°	26.7°	2,3
114B	14:07	86.7°	35.8°	2,4

^aA, MER-A/Spirit; B, MER-B/Opportunity.

^bLocal True Solar Time of MGS passage over the latitude of the rover.

^cMaximum elevation angle (in “local level” coordinates) of MGS as viewed by the rover.

^d1, N-S Mini-TES sequence (see text); 2, elevation scan, single azimuth; 3, offset from overflight, Mini-TES obtained at 12:35 LTST; 4, offset from overflight, Mini-TES sequence, obtained at 12:28 LTST.

Thermal Emission Spectrometer (Mini-TES) and near-simultaneous optical imaging by the Panoramic Camera (Pancam). The ideal sequence contains a series of Mini-TES integrations that begin at an elevation angle of 30° at the moment MGS passes through the spectrometer’s 20 milliradian field of view (traveling from south to north). The instrument continues its observations along the southern azimuth of the MGS track, but includes several elevation angles (typically 30°-20°-10° and then back to 30°). As MGS reaches its maximum elevation angle, the Mini-TES aperture is slewed to the northern azimuth that will contain the MGS in the field of view at an elevation angle of 30°. An additional scan in elevation is made at this same azimuth. The overflight campaigns usually include Pancam solar and sky survey imaging sequences [Lemmon *et al.*, 2004], either directly before or after the Mini-TES block. Practical tactical constraints can modify the precise nature from that described above, but the first four overflights listed in Table 1 executed without significant deviation. A series of unfortunate events precluded rover implementation of this exact sequence for sols 115A (MER-A/Spirit sol 115) and 114B (MER-B/Opportunity sol 114). However, at least one Mini-TES sequence is available for a local time within 1.5 hrs of each of these two overflight.

[11] The instruments involved in our work are described quite comprehensively in the literature. Accordingly, we give the relevant citations, providing additional information for cases when it is not available in published form, as well as for considerations of the reader’s convenience.

2.1.1. Mini-TES

[12] The Mini-TES is a Fourier Transform Spectrometer that covers the spectral range from ~ 340 – 2000 cm^{-1} with a spectral resolution of 12.6 cm^{-1} and a spectral sampling interval of 10.0 cm^{-1} . Because of signal-to-noise issues, we restrict our analyses to the 340 – 1300 cm^{-1} frequency range. General design, operational, and performance characteristics are detailed by Christensen *et al.* [2003, 2004a, 2004b], including some updates that reflect instrumental changes after the commencement of landed operations. However, our analyses employ Mini-TES data that have been calibrated with software which departs from that developed by the Mini-TES team at Arizona State University (ASU) in that it accounts for changes in the instrumental response function, as described by Smith *et al.* [2006].

[13] Mini-TES acquires spectra in approximately 2 second intervals, or ICKs (Integration Counter Keeper). Although

an onboard co-addition capability exists, the standard operating procedure is to return data from each ICK. Thus the user retains the option to analyze all spectra separately or to apply standard co-addition techniques. In this paper, we opt for the latter approach where the summed spectra generally contain 100 ICKs for each pointing (i.e., unique combination of elevation and azimuth angles). In addition, we focus on the atmospheric observations that contain a single azimuth and three elevation angles, the so-called “elevation scan.” Other types of observations are described by Smith *et al.* [2006].

[14] For the issue of measurement error, one might wish to start with the instrumental Noise Equivalent Spectral Radiance (NESR) [Christensen *et al.*, 2003]. However, the process of scaling the NESR to different instrumental and scene temperatures appears fraught with peril. Furthermore, considering our desire to maximize the signal-to-noise through the use of co-addition, we take a more empirical route. For each Mini-TES pointing, we co-add the data using a simple arithmetic mean, employing the resulting standard deviation (root-mean-square, rms) as the error. Figure 1 displays an example of the process, revealing that error bars get larger where expected and appear to encompass point-to-point scatter in the data themselves. In fact,

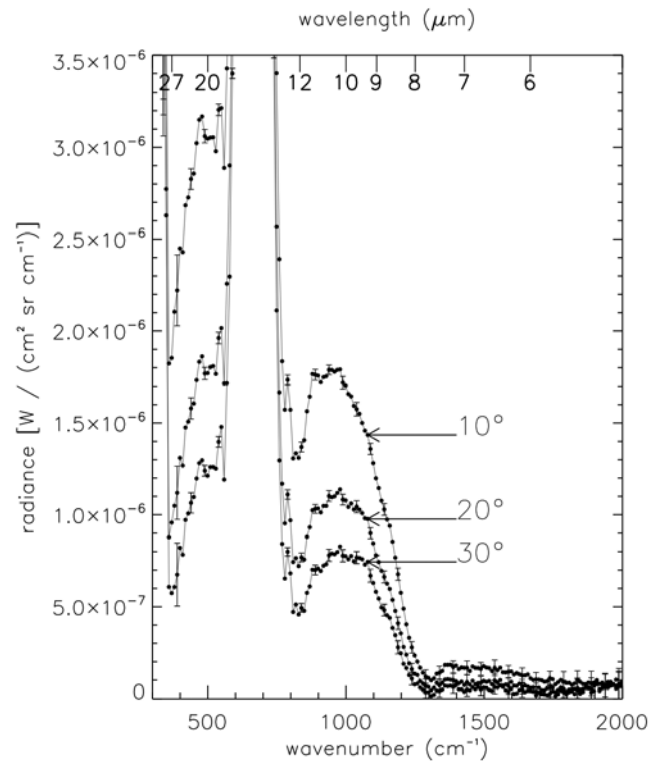


Figure 1. Mini-TES elevation scan obtained on Sol 46A at 13:17 Local True Solar Time (LTST), with the individual elevation angles (local level) labeled. The plotted spectra are averages over the entire 100 ICK dwell time at each angle. The error bars represent the standard deviation (root-mean-square, rms), with every fifth error bar plotted. To preserve legibility of the error bars, we clip the data in the 667 cm^{-1} CO_2 band. The relative size of the error bars appears relatively constant across elevation angle. This can be more clearly seen in Figure 2.

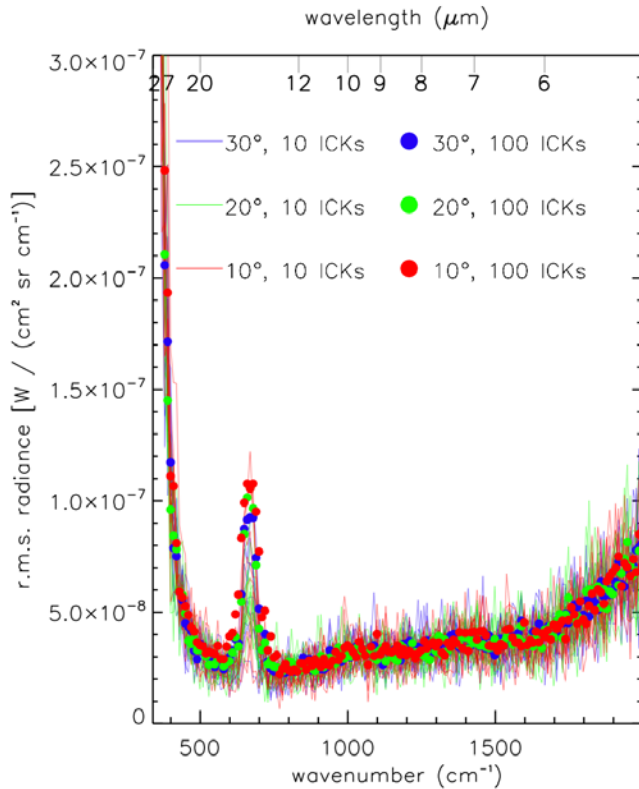


Figure 2. Demonstration of the error measure. We display the standard deviation (rms) for the data shown in Figure 1, calculated with both a 10 ICK and 100 ICK co-addition. For the 10 ICK sampling, there are 10 rms spectra plotted for each elevation angle. With the exception of peak in the 667 cm^{-1} region, the general shape and amplitude are similar to those of the 0° C case of the noise-equivalent spectral radiance (NESR) shown by *Christensen et al.* [2003, Figure 12].

the amplitude of the rms seems to be rather similar among the different elevation angles, despite a factor of about three in the range of absolute radiance. Figure 2 better illustrates this approximate consistency of the rms for a given frequency (i.e., wavenumber; we will use the two terms interchangeably).

[15] The viability of the empirical approach may be evaluated with comparisons of the resulting rms radiance to the Mini-TES pre-flight calibration data. Inspection of the rms spectra derived from the 10 ICK and the 100 ICK sampling windows demonstrates both the improvement (reduction in scatter) and the limitation (same mean rms values) of co-addition. We interpret these two trends as being indicative of the random (precision) and systematic (accuracy) components of the error, respectively. The general shape of the data as a function of frequency in Figure 2 is in very good agreement with the measurements of the NESR [*Christensen et al.*, 2003, Figure 12]. The mean amplitude, whose general invariance we are interpreting as being indicative of the systematic error component, is consistent with previous estimates of the absolute radiometric accuracy [e.g., *Christensen et al.*, 2003, 2004a, 2004b]. Repetition of this exercise for a group of spectra which span the range of atmospheric radiance values (e.g., using higher

elevation angles, data taken at night and during the peak of aphelion/perihelion seasons) shows the same correspondence: reduced scatter with co-addition and a mean component which does not differ appreciably with additional averaging. The peak in the 667 cm^{-1} region is the sole significant departure from the shape of the pre-flight NESR data, and is the result of actual atmospheric variability, even on the 10 ICK timescale [*Smith et al.*, 2006]. We have not (yet) detected similar variability associated with aerosols, at least on the scale of 100 ICKs. As a result of this non-detection and our focus on aerosol retrievals, we ignore the possibility of atmospheric variability on a timescale of the observation execution time. Ultimately, we adopt the rms spectrum as the observational error.

2.1.2. Pancam

[16] The Pancam instrument is a multi-spectral imaging system that contains two digital cameras, each with a $16^\circ \times 16^\circ$ field of view (0.27 milliradians per pixel). Here, our main interest in Pancam is its ability to directly image the sun, providing a robust measurement of the total extinction optical depth. *Bell et al.* [2003, 2006] describe the relevant design and operational characteristics, as well as the detail of the calibration process and radiometric performance. Although the instrument design specification allows for solar imaging at $0.44\text{ }\mu\text{m}$ (L8 filter) and $0.88\text{ }\mu\text{m}$ (R8 filter), a “red leak” in the blue filter gives L8 an effective wavelength of $\sim 0.7\text{ }\mu\text{m}$ [*Lemmon et al.*, 2004]. For the purposes of our analyses and the span of time to be considered, we do not find the two data sets to differ significantly beyond their relative uncertainties, and thus restrict our attention to the better characterized R8 data. We incorporate the relevant R8 optical depths from the results of *Lemmon et al.* [2004] for the desired sols.

2.2. MGS-TES

[17] Within the context of this paper, the TES emission phase function (EPF) sequence is the MGS core contribution to the overflight campaign. Although the concept of the EPF was introduced during the Viking Orbiter mission to study the directional dependence of surface thermal emission processes, it is better known for its utility in aerosol characterization studies [*Kieffer et al.*, 1976; *Clancy and Lee*, 1991; *Clancy et al.*, 2003b]. Of particular merit, as shown by *Clancy et al.* [2003b], the monochromatic solar-band EPF data can often discriminate between aerosol types despite the inherent lack of spectral resolution. As for the IR data, the sampling scheme is such that, in principle, one obtains additional leverage on both surface and atmospheric properties relative to that solely from nadir data. However, the combination of pointing drift and non-Lambert surface emissivity [e.g., *Bandfield and Smith*, 2003; *Wolff and Clancy*, 2003, section 4.6] can complicate the analyses to the point that one considers only the nadir data.

2.2.1. IR Spectrometer

[18] A description of the TES spectrometer and its radiometric performance may be found in several publications with the most comprehensive report presented by *Christensen et al.* [2001]. We employ the same algorithm to describe the observational errors as in our earlier work [*Wolff and Clancy*, 2003, section 3]: the NESR values (for a single detector, $2.5 \times 10^{-8}\text{ W cm}^{-2}\text{ sr}^{-1}\text{ cm}^{-1}$ from 300 cm^{-1} to 1400 cm^{-1} ; $6 \times 10^{-8}\text{ W cm}^{-2}\text{ sr}^{-1}\text{ cm}^{-1}$ at 250 cm^{-1} ; $4 \times$

$10^{-8} \text{ W cm}^{-2} \text{ sr}^{-1} \text{ cm}^{-1}$ at 1450 cm^{-1} ; linear interpolation used for $250\text{--}300 \text{ cm}^{-1}$ and $1450\text{--}1600 \text{ cm}^{-1}$ ranges) added in quadrature with a radiance (accuracy) uncertainty ($1 \times 10^{-8} \text{ W cm}^{-2} \text{ sr}^{-1} \text{ cm}^{-1}$). We typically use the in the $250\text{--}1400 \text{ cm}^{-1}$ range (all in 10 cm^{-1} sampling model) and co-add 3–6 sequential ICKs with six pixels each. However, in an effort to allow for additional systematic effects, we compute the NESR term using only 25% of the number of spectra (under the assumption of Poisson statistics). That is to say, co-adding 36 spectra reduces the NESR by only $\sqrt{9}$.

2.2.2. Solarband Bolometer

[19] *Clancy et al.* [2003b] provide a detailed description of the TES EPF sequences and their applicability to the derivation of total aerosol optical depth. As indicated in that work, the effective wavelength of the solar band is near $0.7 \mu\text{m}$. The EPF data analyzed here are primarily those of the 9-point variety (i.e., emergence angles of $\pm 75^\circ$, $\pm 65^\circ$, $\pm 55^\circ$, $\pm 30^\circ$, 0°), with the remainder being of the “dense” type. *Christensen et al.* [2001] provide additional instrumental and calibration discussion of the solarband bolometer.

3. Modeling Details

[20] While much of the numerical apparatus critical to our work is described elsewhere, some modifications have been made in order to account for the unique aspects of our data set, including the upward-viewing geometry and subsequent input parameter sensitivities. We summarize such changes and clarifications briefly, reviewing previously described facets only when it is likely the reader will benefit.

3.1. Algorithms

[21] The retrievals performed here generally embody two distinct approaches: (1) fully automated as in the case of the TES IR and Mini-TES analyses and (2) interactive “fitting of the data” as in the case of the TES solar band, both EPF and limb. At the core of these methodologies, one finds radiative transfer and minimization algorithms (although in the case of approach 2, the algorithm is a manual χ^2 reduction process).

3.1.1. IR Radiative Transfer

[22] We perform the IR radiative transfer with REFLEX, the doubling-adding code originally developed by *Gladstone et al.* [1984] for terrestrial applications, and subsequently modified for analysis of Martian atmospheric observations [*Clancy et al.*, 1995; *Wolff and Clancy*, 2003]. We have made additional modifications to allow for the analysis of the Mini-TES data: a pseudo-spherical geometry (a Chapman function instead of the classical plane-parallel secant factor [e.g., *Thomas and Stamnes*, 1999, Appendix L]), and a vertical mesh with finer sampling near the surface in Mini-TES “mode” (40 points with logarithmic sampling of altitude between 1.5 m and $\sim 25 \text{ km}$, 15 points with linear spacing between 25 km and 60 km).

3.1.2. Solarband Radiative Transfer

[23] We model the TES solarband EPF sequences using the approach and numerical algorithms of *Clancy et al.* [2003b]. The core of the radiative transfer is the public domain discrete-ordinates DISORT package developed and maintained by *Stamnes et al.* [1988]; see also discussion by *Thomas and Stamnes* [1999]. We assume the presence of a single type of aerosol, leading to the “retrieval” of a best-fit

phase function (from a sample of two dust and two water ice end members), a total optical depth, and an effective particle single scattering albedo. The only departure from the implementation of *Clancy et al.* [2003b] is that we employ a fixed, “atmospherically corrected” normal albedo as discussed below. We still adjust the normal values by either the “bright” or the “dark” surface phase functions used by *Clancy et al.* [2003b].

3.1.3. Least Squares Minimization

[24] The minimization engine for the IR retrievals is the IDL-based MPFIT routines developed by Craig Markwardt (<http://cow.physics.wisc.edu/~craigm/idl/idl.html>). The MPFIT code is based upon the well-known and tested MINPACK-1 FORTRAN minimization library [*Moré et al.*, 1984]. The features of MPFIT include the ability to bound parameter values, to control step-sizes, and to calculate either one-sided or two-sided numerical derivatives for the Jacobian. The TES-mode of the “driver” implementation operates as discussed by *Wolff and Clancy* [2003]. For the Mini-TES analyses, we added the capability to perform retrievals simultaneously from multiple spectra, such as those obtained in an elevation scan. The figure of merit for convergence is the traditional χ^2 statistic weighted by the observational errors: i.e., $\chi^2 = \sum((data - model)/\sigma_{obs})^2$. The retrieved parameter uncertainties are calculated directly from the diagonal of the covariance matrix.

[25] The Mini-TES general procedure involves multiple calls to MPFIT. Initially, one examines only a subset of the data, typically the $1000\text{--}1300 \text{ cm}^{-1}$ range, and fixes most of the potential parameters, retrieving $\tau_{1075,dust}$ and T_{surf} . This initial analysis is the result of the need to update the measured surface temperature (see also section 4.2). A second call is made for the full wavenumber range and allows the determination of $\tau_{1075,dust}$, T_{surf} (but is bounded to be $\pm 5 \text{ K}$ from the first call), and optionally, r_{eff} and a parameterization of the vertical mixing profile.

3.2. Particle Cross Sections

[26] Scattering properties for the solarband analyses are not need to be computed explicitly from first principles, i.e., we retrieve the best-fit normal-incidence optical depth and single-scattering albedo while testing phase functions from a pre-determined set. Implicit in this approach is that set of scattering properties are representative of the aerosols in a given observation. We limit ourselves to those derived by *Clancy et al.* [2003b], and note that *Wolff and Clancy* [2003] showed that the dust properties do not appear to vary in the general geographical regions of interest to this paper (except possibly during large dust storms). For the thermal IR, we have previously illustrated the general insensitivity of forward-scattering parameters on the exact nature of the aerosol particle shapes [*Wolff and Clancy*, 2003], as well as discussed the impact on the scattering phase function. However, given the importance of scattering for the Mini-TES viewing geometry, we wish to re-examine the phase function aspect. Figure 3 shows the dependence of the normalized phase functions in two different frequency regimes for a canonical dust size distribution, as characterized by the first two moments of the distribution, $r_{eff} = 1.5 \mu\text{m}$ and $v_{eff} = 0.4$ [*Hansen and Travis*, 1974]. We choose a shape which reasonably reproduces the empirically derived function of *Tomasko et al.* [1999]; that is to say a randomly

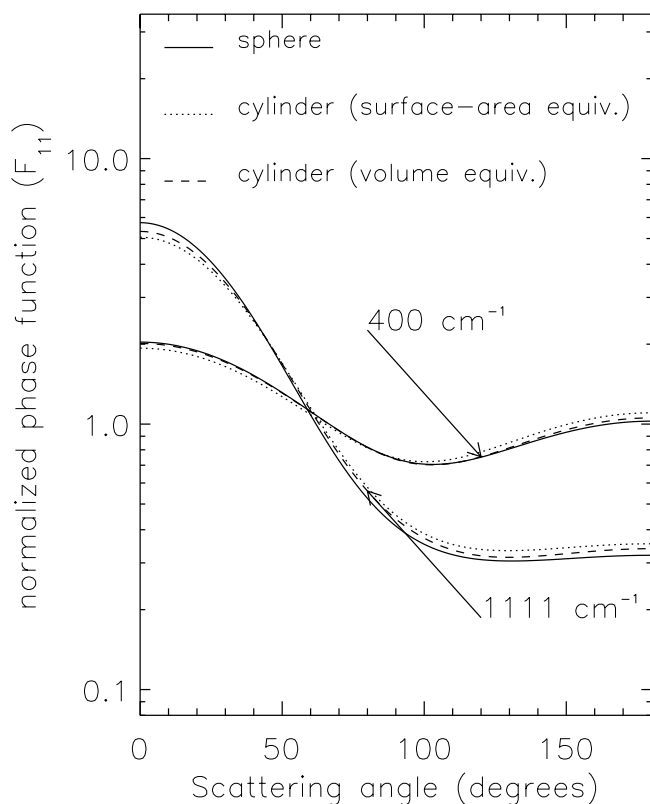


Figure 3. Scattering phase functions for a typical dust aerosol distribution ($r_{eff} = 1.5 \mu\text{m}$, $v_{eff} = 0.4$) at 1111 cm^{-1} ($9 \mu\text{m}$) and 400 cm^{-1} ($25 \mu\text{m}$). Although the phase functions of volume equivalent non-spherical particles are a more appropriate comparison to Martian atmospheric aerosols than are spheres, both non-spherical equivalents show a maximum of $\sim 10\%$ departure from the sphere case. This difference decreases appreciably for longer wavelengths. The indices of refraction derived in this work are used (e.g., Figures 15 and 16).

oriented oblate cylinder with a 2:1 axial ratio [e.g., *Wolff et al.*, 2001]. The cylindrical particle properties are computed using the T-Matrix code, TMQ, of Michael Mishchenko and collaborators (<http://www.giss.nasa.gov/~crmim/>) for both the volume- and surface-equivalent cases. Although the volume-equivalent case is more relevant for the Mini-TES frequency regime, both cases show departures from the spherical case by at most $\sim 10\%$, with the longer wavelengths demonstrating generally much smaller differences. As a result, we can adopt the much more computationally efficient spherical shape (at a CPU-time savings measured on the order-of-magnitude scale) without introducing systematic effects above the $\sim 5\%$ level in radiance over the $\sim 250\text{--}1250 \text{ cm}^{-1}$ range.

3.3. Surface Emissivity and Normal Albedo

[27] As mentioned above, the off-nadir spectra can contain systematic effects that significantly complicate analyses, in particular in the IR. More specifically, the moderate-to-bright surfaces near both rover sites are those most likely to contain directional emissivity effects [e.g., *Pitman et al.*, 2006]. In addition, the “smearing” of the detector footprint

in the along-track direction can enhance the difficulty one encounters with the mixing of several emissivity spectra in a single pixel/region, and the variability of the phenomenon across the angles in the EPF sequence. Consequently, we adopt the nadir-only approach of *Wolff and Clancy* [2003], with the modification that we sample from emissivity maps binned at both 2 and 4 pixels per degree, where the former bin-size is used for the case of “no data” in the latter (higher resolution) bin. An additional enhancement in the emissivities over that described by *Bandfield* [2002] is a more accurate treatment of the small CO_2 absorption features found on the shortwave side of the 667 cm^{-1} band.

[28] We utilize an “atmospherically corrected” Lambert albedo for the solarband EPF analyses (a discussion of the details of the correction methodology may be found in Appendix A). We map-project the corrected albedo values into a region $10^\circ \times 10^\circ$ centered on each rover landing site, using a bin-width of 64 pixels per degree. The amplitude of the correction is largest over darker surfaces. Within the sol 22B EPF (near the Opportunity site), the effects of the atmosphere at nadir are $\sim 20\text{--}30\%$, with corrected albedo values in the 0.10–0.12 range. They are typically much smaller over brighter regions, e.g., $\lesssim 10\text{--}15\%$ for albedo values near 0.2. An additional advantage in the generated maps is the spatial resolution, which can explicitly account for dispersion that occurs as a result of the pointing limitations of the TES EPF [*Bandfield and Smith*, 2003] and the intrinsic albedo variability found near both rovers. Although not always dramatic, the general improvement in the EPF analyses resulting from the new surface albedo treatment may be found in the increased precision of the retrieved optical depth and a single-scattering albedo.

4. Mini-TES Sensitivity Studies

[29] The Mini-TES data form a critical aspect of our work. Given its unique perspective on the Martian atmosphere, one should consider the degree to which various radiative transfer inputs differ from those previously explored for TES [cf. *Wolff and Clancy*, 2003]. We examine briefly a few of the more interesting (and important) ones.

4.1. Scattering

[30] Atmospheric analyses of TES (disk-viewing) data are often able to employ the non-scattering or “absorbing” atmosphere approximation [e.g., *Hanel et al.*, 2003, section 2.4] to represent the radiative effects of the atmosphere [cf. *Bandfield et al.*, 2000; *Smith et al.*, 2000]. That is to say, as long as one realizes that the optical depths retrieved in such an approach are not the same as the extinction optical depth, one may compare results from such an approximate approach with those from a full multiple-scattering analysis: $\tau_{abs} \simeq (1 - \omega) \tau_{ext}$, where ω is the aerosol effective single scattering albedo [e.g., *Wolff and Clancy*, 2003]. The applicability of the non-scattering algorithm for the Martian atmosphere in the thermal IR depends upon the relative contribution of the scattered light with respect to that of the emitted component. For TES observations of the surface (and the intervening atmosphere), one finds $\frac{\text{scattered radiance}}{\text{emitted radiance}} \ll 1$ generally to be true, as can be seen in Figure 4. While one might hope that the same applies to Mini-TES observations of the sky, an inspection of the figure clearly reveals that not

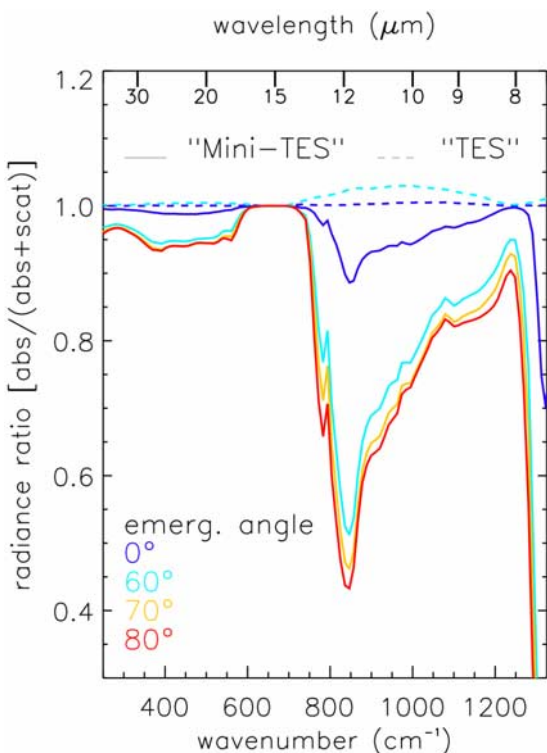


Figure 4. The effect of scattering: TES versus Mini-TES observing geometries. Synthetic spectra are calculated using the temperature profile from the Sol 46A overflight and $\tau_{dust,ext} = 0.3$ (with properties as those in Figure 3) for several atmospheric slant paths. For convenience, we give only the emergence angles as defined for TES viewing geometry; for Mini-TES atmospheric viewing, $e_{Mini-TES} = 180^\circ - e_{TES}$. The ratio plotted is that of the “absorbing atmosphere” radiance relative to the full multiple scattering radiance. The solid lines represent the Mini-TES view (downwelling), while the dashed lines show the TES view (upwelling). The relative importance of scattering between the two viewpoints is quite distinctive.

to be the case (with the exception being found at the center of the highly absorptive 667 cm^{-1} CO_2 band). Figure 4 shows the radiance from the “absorbing atmosphere” model relative to that of the full extinction model for several viewing angles (TES: $e = 0^\circ, 60^\circ$; Mini-TES: $e = 180^\circ, 120^\circ, 110^\circ$, and 100° corresponding to elevation angles of $90^\circ, 30^\circ, 20^\circ$, and 10° , respectively) with the same dust aerosol model as employed in Figure 3. Clearly, given the departure of the ratio from unity, one must account for the presence of scattering in Mini-TES atmospheric analyses outside of the 667 cm^{-1} band center.

4.2. Surface Temperature and Emissivity

[31] The demonstrated importance of the atmospheric scattering process for Mini-TES observations invokes a degree of concern regarding the properties of the radiation emitted by the surface. In other words, we need to examine the effects of variations (or errors) in specifying the surface temperature and emissivity for terrain surrounding the rovers. Figure 5 shows the impact of differing surface temperatures on a simulated Mini-TES elevation scan using

the previously defined atmospheric conditions (e.g., for Figure 4). Although changes in surface temperature can clearly alter the spectral behavior, particularly for lower elevation angles, a large error in the temperature would be required for a significant effect. For a given observation, we calculate an average surface temperature from all surface observations within a ± 45 minute local time window for a period typically spanning ± 5 sols (for the case of less than 20 observations, the sol-window is expanded to ± 10). To derive surface temperature, we use a simple inversion of the Planck function for data averaged over the $1300\text{--}1400\text{ cm}^{-1}$ ($450\text{--}500\text{ cm}^{-1}$ can be used for cold surface conditions such as early morning or evening). Generally, the standard deviation of this approach is at most 1–2 K, though it can be $\sim 3\text{--}4$ K if the targets include rocks. Figures 6 and 7 clearly demonstrate the insensitivity of atmospheric Mini-TES data to the exact spectral nature of the adopted surface emissivity. However, for consistency, we adopt an average of the emissivity spectra near the rover locations from the four pixel-per-degree maps described in section 3.3. Of course, what we really need to know is the spatial integral over the surface emission processes. In addition, the viewing geometry is such that radiation emitted at large angles is more preferentially scattered into the Mini-TES field-of-view. Accordingly, the issue of directional emissivity can arise. While each may affect the radiation field at the level of a few degrees Kelvin, we account for this

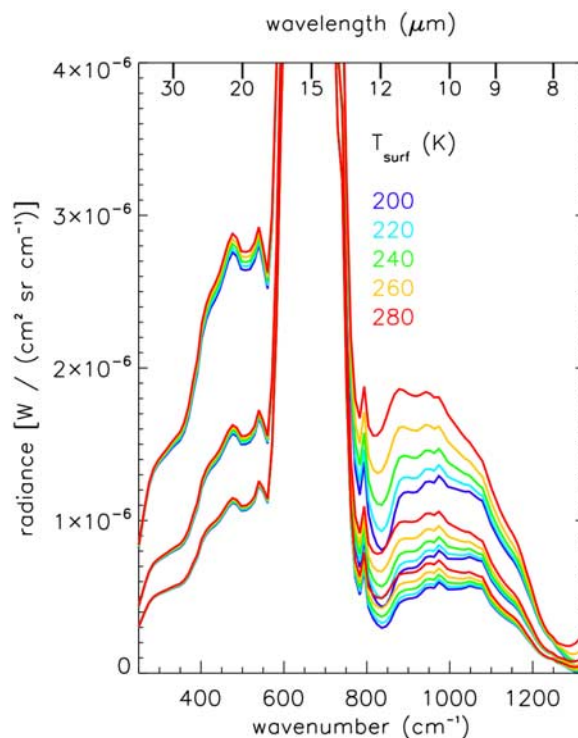


Figure 5. The effect of surface temperature on Mini-TES radiances. Synthetic spectra are calculated for a wide range of surface temperatures under the assumption of a unit surface emissivity at a temperature of 270 K. The atmospheric conditions are the same as those in Figure 4. The three groups of spectra represent the elevation angles 10° (largest radiances), 20° , and 30° (smallest radiances).

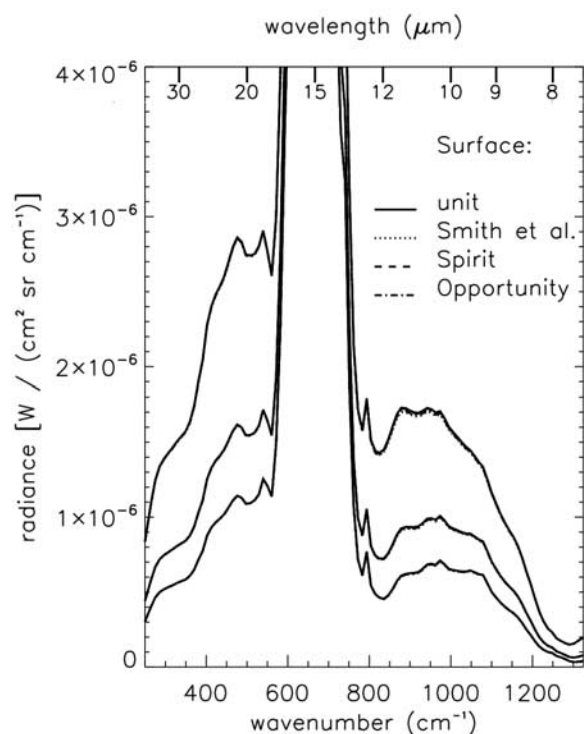


Figure 6. The effect of surface emissivity on Mini-TES radiances. As for Figure 5, but for a surface temperature of 270 K and a sample of 4 emissivity spectra. We include representative emissivity data (see Figure 7) from both rover locations (as sampled by TES; see text and *Bandfield* [2002]), that employed by *Smith et al.* [2000], and that of a constant value (of unity). Given the extremely low sensitivity of the model radiances to the exact emissivity spectrum adopted, we expect no measurable impact on our retrievals from Mini-TES data.

unknown quantity by allowing a bounded iteration on the surface temperature parameter.

4.3. Temperature Profiles

[32] As a rule, we adopt the temperature vertical profiles ($T(p)$) from the work of *Smith et al.* [2004, 2006], who provide a full description of the methodology, uncertainties, and caveats associated with the profiles. The actual input to the radiative transfer retrievals, $T(z)$, is derived from the conversion of pressure levels to altitudes by integrating the hydrostatic equation. Although most of our work here concerns itself with overflight data (including the daily afternoon overpasses, not just the special coordinated campaigns), we briefly explore the potential limitations of aerosol retrievals for Mini-TES observations at local times not sampled by MGS overflights. In other words, one might ask about whether there could be concerns for the case of the initial “guess” of $T(p)$ provided by MGS/TES sampling a local time more than a few hours (or so) from that of Mini-TES.

[33] Figure 8 provides some typical contribution functions for Mini-TES and TES at an elevation angle of 30° and at nadir, respectively. In addition to the obvious complementary nature of the combined sensitivity altitude range for $T(p)$ sounding (as portrayed by the solid lines,

representing wavenumbers in the 667 cm^{-1} CO_2 band), the figures highlight the fact that the aerosol contribution functions (dashed lines) for Mini-TES lie primarily at altitudes *above* the validity range of the Mini-TES $T(p)$ (~ 2.5 km, horizontal blue dotted line). Although the plotted contribution functions embody the non-scattering atmosphere approximation, the effects of scattering, at least at the optical depths observed thus far by the rovers, are not adequate to decouple the observed radiance from the atmospheric temperature above the canonical $\sim 2\text{--}3$ km limit, not even for elevation angles near 10° . In other words, it appears that aerosol retrievals from Mini-TES data will require an additional source of information. This can be perhaps better illustrated with the results of a simple experiment: we perform the same retrieval as *Smith et al.* [2006], using the same algorithmic implementation, with a series of TES-derived $T(p)$ as the initial guess. Initially, we choose the “best” or “closest” TES measurement, moving onto $T(p)$ from what might be considered potentially quite different atmospheric conditions: night time, the opposite side of the planet, and several months later. Figure 9 shows the results (lines) of the experiment for an observation during the sol 46A overflight using a TES profile (filled circles) from that coordinated campaign along with those from the nights of sols 33B, 102A, and 133B. We carry out a second trial for an observation from the morning of sol 46A, a time well outside of the MGS overflight period. While the $T(p)$ for altitudes below (pressures above) the

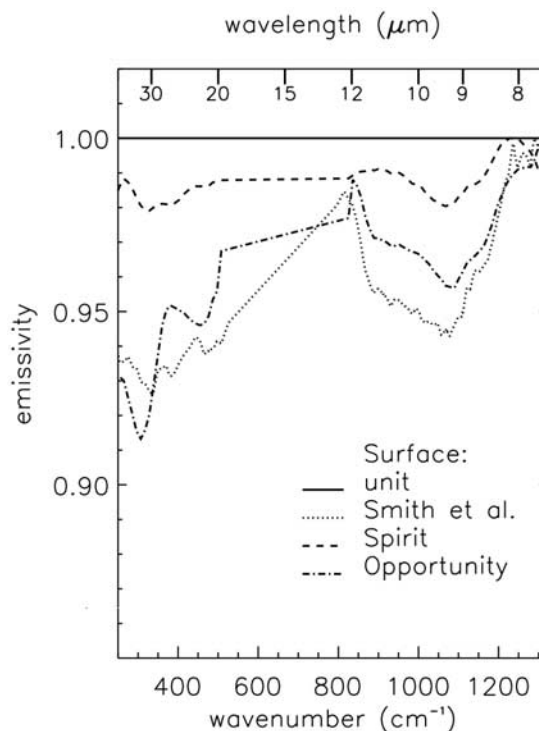


Figure 7. Surface emissivity sample used for sensitivity analysis shown in Figure 6. The representative Gusev Crater and Meridiani Planum emissivity data are bracketed by the more extreme cases of a constant (unity) value and that employed by *Smith et al.* [2000, Figure 13]. All four cases produce essentially indistinguishable atmospheric model spectra (see Figure 7).

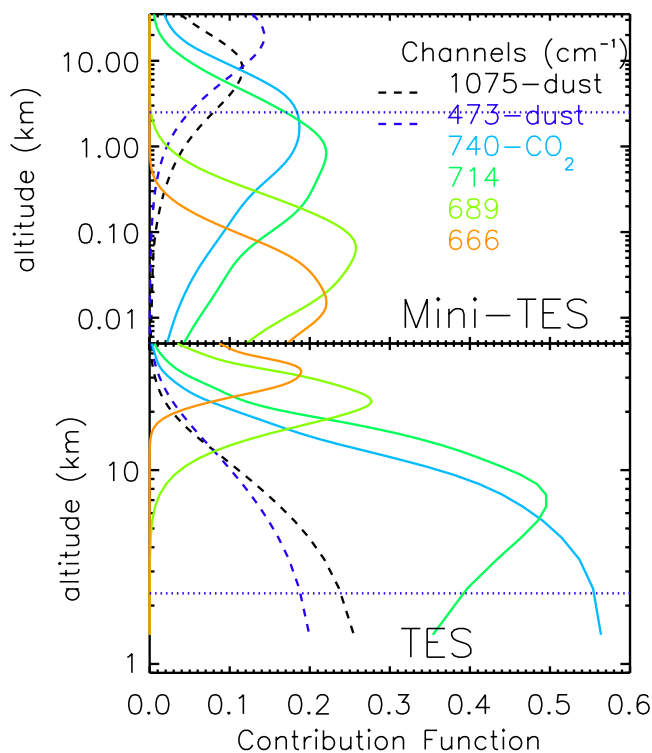


Figure 8. Typical contribution functions for (top) a Mini-TES and (bottom) a TES observation. The Mini-TES geometry is an elevation angle of 30° , while that for TES is nadir. The wavenumber for each profile is color-coded, with the solid lines representing the CO_2 band and the dashed lines sampling the centers of short- and long-wave dust features. The horizontal dotted line shows the approximate limiting altitude of the Mini-TES temperature profiles (~ 2.5 km [Smith *et al.*, 2006]). Contribution functions are just the weighting functions scaled by a derivative of the Planck function [e.g., Hanel *et al.*, 2003, chap. 8; see also Conrath *et al.*, 2000; Smith *et al.*, 2006]. The altitude scale is derived by integrating the hydrostatic equation of state using TES $T(p)$ data representative of conditions in the equatorial and middle latitudes during early southern summer (OCK 4242, ICKs 1629–1631, $L_S = 218^\circ$).

upper sensitivity limit are fairly insensitive to the initial guess, the retrieval simply follows the TES profile for altitudes above 3–4 mb (~ 7 –10 km), where much of the aerosol radiance originates (e.g., Figure 8). That is to say, *the retrieval of aerosol properties from Mini-TES data is explicitly linked to $T(p)$ at altitudes above those which Mini-TES is sensitive to $T(p)$!*

[34] The connection between the adopted $T(p)$ and the model radiance due to aerosols manifests itself at two levels: the spectral shape and 1075 cm^{-1} dust optical depth ($\tau_{1075,dust}$). As can be seen in the retrieved optical depths from our temperature experiment, the parenthetical values in the legend of Figures 9 and 10, the ~ 15 K difference between the TES sol 46A case and those of sols 102A and 137B produces errors in $\tau_{1075,dust}$ at the 20% level. The smaller perturbation represented by the sol 33B TES profile (relative to that of 46A) introduces an error at the level of only a few percent. While these results are consistent with

those reported by Smith *et al.* [2006], the relatively modest uncertainty that one might perceive in $\tau_{1075,dust}$ due to errors in $T(p)$ masks the more insidious issue of frequency-dependent effects. In other words, in addition to the demonstrated error in the retrieved dust column, the choice of an incorrect $T(p)$ leads to an inaccurate spectral representation of aerosols.

[35] This second connection between $T(p)$ and aerosol radiance originates in the non-linear nature of the Planck function and the differing contribution functions for the short- and long-wave frequencies. A perturbation in the $T(p)$ above 5 km introduces a change in the spectral shape of the radiance that mimics microphysical effects, such as changes in particle size or composition (indices of refraction). While

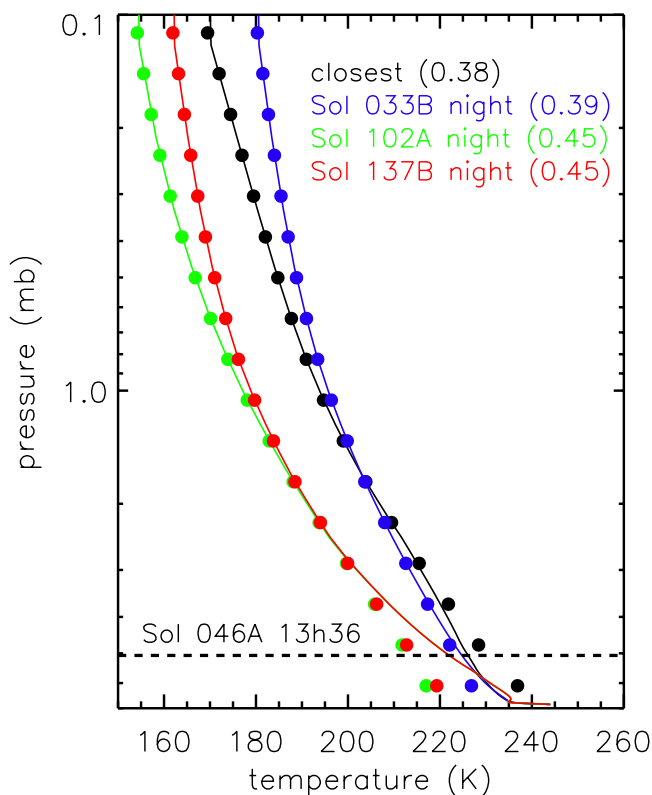


Figure 9. Retrieved $T(p)$ of an overflight block Mini-TES observation using four TES retrievals as “initial guesses” (lines). The departure of the TES profiles (lines) from those of Mini-TES (circles) below the 4–5 mb level clearly illustrates the sensitivity range of the Mini-TES observations. Conversely, the coincidence of the circles and lines demonstrates the inability of Mini-TES to constrain $T(p)$ in this region; this has significant implication for the analyses of Mini-TES data at local times well away from the TES overflight blocks. The numbers in parentheses give the associated 1075 cm^{-1} optical depth. The horizontal black dashed line gives the upper sensitivity limit of $T(p)$ (~ 2.5 km). The Mini-TES observation is that from the coordinated overflight on sol 46A, and the adopted TES data are taken from four different overflights: sol 46A as well as the nighttime passes of sol 33B, sol 102A, and sol 137B. The motivation for the latter three data sets is the choice of potentially very different atmospheric conditions. We perform the computations using the code of Smith *et al.* [2006].

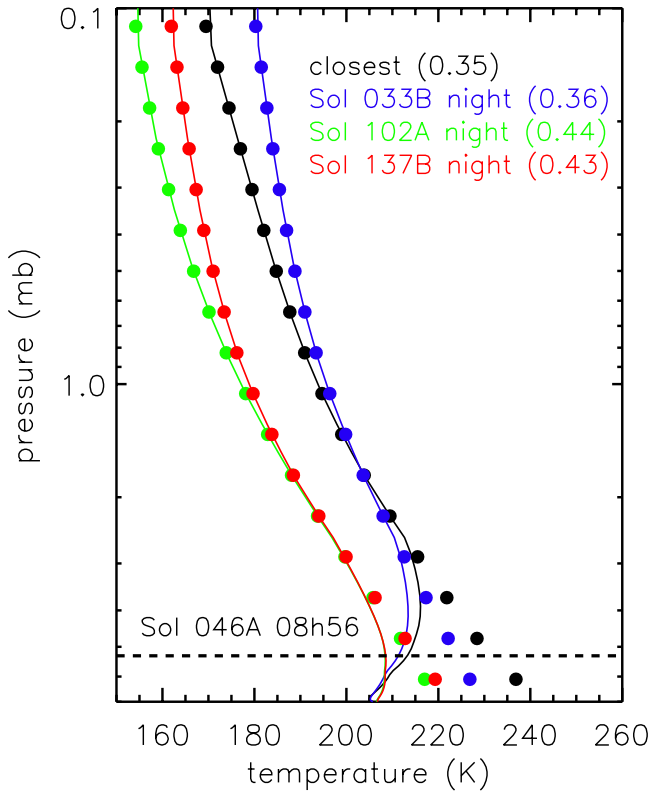


Figure 10. Retrieved $T(p)$ of a morning Mini-TES observation using four different TES retrievals as “initial guesses.” With the exception of the Mini-TES data coming from the morning of sol 046A, the details are the same as those for Figure 9.

our previous experiment was designed to encompass potentially extreme perturbations, there is no database of retrieved $T(p)$ with the necessary diurnal, vertical, and spatial coverage to allow one to assess more precisely the most probable or average $T(p)$ for a given date and time. While Mars Global Circulation Models (MGCMs) do provide some guidance in estimating diurnal effects, in terms of actually observations, we have only the TES $T(p)$. As such, their range of applicability represents a fundamental limitation for Mini-TES aerosol analyses.

[36] To eliminate as much uncertainty as possible for deriving optical properties, we classify our Mini-TES data into three bins on the basis of local time of the TES profile:

[37] 1. Within 30 minutes of the highest elevation angle of MGS overflight itself, near the local time block of the overflight. This is the interval where one assumes the TES $T(p)$ is strictly valid. From here, we draw the data for deriving the indices of refraction.

[38] 2. $\sim 12:00$ – $15:00$ (the “MGS-block”). On the basis of $T(p)$ from a Mars Global Circulation Model (MGCM) for conditions appropriate to Gusev and Meridiani early in the mission, kindly provided by R. John Wilson [e.g., *Hinson and Wilson*, 2004], we anticipate small to modest errors with respect to the $T(p)$ provided by the early afternoon TES overpass.

[39] 3. The remaining data. The MGCM profiles indicate a greater departure in temperatures from the times sampled

by closest TES $T(p)$. When plotting retrieval results, this sample will be flagged with a unique symbol.

4.4. Dust Vertical Distribution

[40] The dust vertical distribution, both in terms of the volume mixing ratio (with respect to CO_2 gas) and the particle microphysical properties, remains a complicating factor. We begin by choosing the mixing ratio parameterization of *Conrath* [1975]: $q(z)/q_0 = \exp(\nu(1 - \exp(z/H)))$, and illustrate the effects of variations in ν (under the assumption of $H = 10$ km) in Figure 11. Here, $q(z)$ is the volume mixing ratio of dust particles to CO_2 molecules; H is the characteristic dust scale height; and ν is defined as the ratio of the characteristic aerosol diffusion to settling times (see *Conrath* [1975] for additional discussion of definitions). The oft-employed “uniform mixing” scheme ($\nu = 0$) would be represented by a vertical line at $q(z)/q_0 = 1$. Recalling the Mini-TES contribution function of Figure 8, one might expect that there should be very little effect on $\tau_{1075,dust}$ for $\nu \lesssim 0.1$. In fact, this is borne out via numerical experimentation (assuming constant dust size, r_{eff}): $\tau_{1075,dust}$ decreases by $\simeq 10\%$ from $\nu = 0.0$ to 0.1 ; and by less than 5% over the range $\nu = 0.00$ – 0.05 . For the TES retrievals, the effect of ν is even smaller, but in the opposite direction, *increasing* by $\lesssim 10\%$ when varying ν from 0.0 to 0.2 . However, the larger ν values might be appropriate for certain conditions (e.g., aphelion conditions where the formation of water ice clouds might provide a “scrubbing” mechanism above the water vapor saturation point; [cf. *Clancy et al.*, 1996]). Consequently, we cannot simply

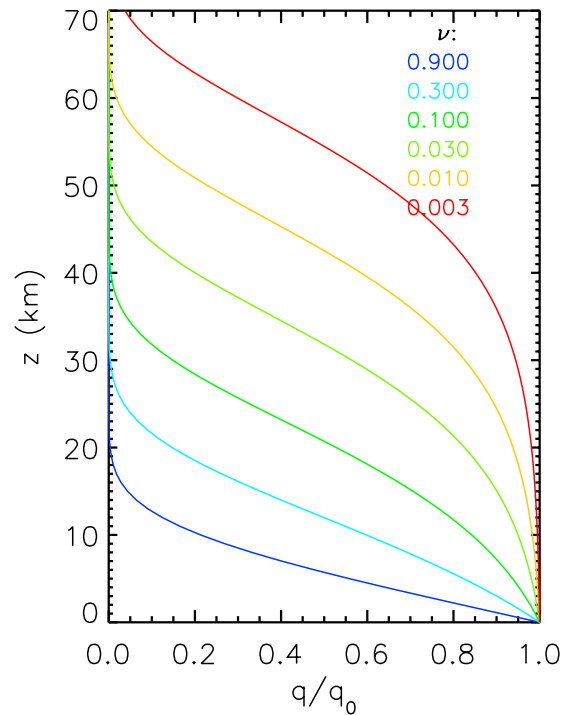


Figure 11. Vertical dependence of aerosol mixing ratios for the parameterization of *Conrath* [1975]. The aerosol mixing ratio $q(z)$ relative to that at the surface (q_0) is plotted for a series of ν values (see text). The canonical “uniform mixing” ($\nu = 0$) would be represented by a vertical line at $q(z)/q_0 = 1$.

Table 2. Coordinated Overflight Retrieval Summary

Sol ^a	TES					MER			
	$\tau_{1075,dust}^b$	$\tau_{825,ice}^b$	T_{surf}^c K	τ_s^c	ω_s^d	Type ^e	$\tau_{1075,dust}^{b,f,g}$	τ_{PANCAM}^b	Vis-IR Ratio
22B	0.38 ± 0.03	0.03 ± 0.02	292.5 ± 0.9	0.90	0.92	3	0.43	0.95 ± 0.02	2.2
46A	0.34 ± 0.03	0.04 ± 0.01	275.9 ± 1.1	0.70	0.92	3	0.37	0.80 ± 0.03	2.2
68B	0.25 ± 0.03	0.03 ± 0.01	284.6 ± 1.0	0.60	0.96	2	0.26	0.70 ± 0.03	2.7
92A	0.19 ± 0.04	0.05 ± 0.01	266.4 ± 1.8	0.50	0.97	1	0.26	0.64 ± 0.02	2.5
115A	0.15 ± 0.02	0.07 ± 0.02	262.1 ± 0.5	0.45	0.97	1	0.25	0.47 ± 0.05	1.9
114B	0.19 ± 0.02	0.04 ± 0.01	276.5 ± 0.5	0.50	0.97	2	0.17	0.61 ± 0.03	3.6

^aA, MER-A/Spirit; B, MER-B/Opportunity.

^bOptical depth defined with respect to normal-incidence column.

^cSolarband optical depth; for all cases precision is ±0.1. This error estimate attempts to embody the systematic effects inherent in the modeling assumptions, including the fixed nature of the adopted surface phase functions [e.g., *Clancy et al.*, 2003b].

^dSolarband (total) aerosol single scattering albedo.

^e*Clancy et al.* [2003b] dominant aerosol phase function types: 1, Ice “Type 1”; 2, Ice “Type 2”; 3, *Tomasko et al.* [1999] dust.

^fUncertainty for tabulated $\tau_{1075,dust}$ is 0.02. In general, it is the maximum of (0.02 for Spirit, 0.03 for Opportunity), 5% of the retrieved value, and the formal parameter uncertainty; the latter can exceed 10% during the aphelion (southern winter) period.

^g $\tau_{825,ice}$ is zero within the uncertainty for all listed epochs.

choose a single vertical mixing ratio function for all cases. Our approach is to consider a single ν value for the initial aerosol analyses that lead up to our updated indices of refraction. Subsequently, we can treat ν as a retrievable parameter.

[41] Vertical variation in an aerosol size distribution would also seem to be a natural consequence of gravitational settling in the atmosphere. Certainly, modeling work in this area indicates that one should expect such behavior. However, outside of some special cases (e.g., occultation geometry, limb observations of discrete cloud structures), direct retrieval of useful particle size constraints as a function of altitude is quite problematic. Thus, although we will address this topic as a “thought experiment” in section 7, our retrievals treat the size distributions as constant with height.

5. Results

[42] When attempting to characterize aerosol properties, particularly those of a microphysical nature such as size, one often resorts to calculating the necessary radiative transfer input parameters from first principles. That is to say, starting with a set of refractive indices, one employs a numerical algorithm to generate the single scattering albedo, the scattering phase function, etc. So, if one possesses the need to derive or improve this fundamental quantity from remote sensing data, one must find an approach that essentially constrains or determines most (if not all) of the other input parameters. With the appropriate data set, one can minimize the number of assumptions. Although one can always find observational data sets lacking in some aspect, the data obtained through the MER-MGS coordinated overflight campaigns embody a reasonable match to the aforementioned ideal.

[43] Our approach is to use the coordinated campaigns to select the appropriately dust-dominated data and provide the necessary constraints on both the particle size distribution and the vertical mixing profile. By “cherry-picking” the appropriate data sets, we can derive the refractive indices with a minimal degree of uncertainty in the menagerie of other radiative transfer input parameters. Once that task is accomplished, one may then proceed with a more general analysis of the Mini-TES data that focuses on dust

loading, particle sizes, and vertical mixing as a function of season (L_S).

5.1. Coordinated Campaign Aerosol Properties

[44] With our emphasis on dust, we choose to focus on the first four months of landed operations in order to avoid the onset of cloud formation associated with the aphelion period. We perform the TES analyses using the basic approaches of *Clancy et al.* [2003b] and *Wolff and Clancy* [2003]. Modifications to those procedures, as well as the general approach for Mini-TES data themselves, are described above. In addition, it is important to understand that the ultimate IR parameters are the result of an iterative process. After deriving an updated set of indices of refraction and particle size constraints, we perform another set of retrievals. For dust, we begin with the refractive indices originally optimized for TES data [*Wolff and Clancy*, 2003, Figure 2]. The final dust size distribution for Mini-TES data, as characterized by r_{eff} and v_{eff} , is given below. For TES, $\tau_{1075,dust}$ is not high enough to provide appreciable retrieval leverage on r_{eff} , particularly given the surface variability near the rovers and the size of the TES footprint. We find $r_{eff} \simeq 1.7$ and $1.9 \mu\text{m}$ for the sol 46A and 22B TES observations, respectively, with a precision of approximately ±0.3–0.4. For water ice, the small values of τ make the exact size distribution less important, and we simply adopt the “Type 1” values of $r_{eff} = 2 \mu\text{m}$ and $v_{eff} = 0.1$ [*Clancy et al.*, 2003b].

[45] Table 2 lists the final retrieved values of both the TES and MER data for the selected campaigns. We wish to highlight several aspects of these results:

[46] 1. The correspondence between the TES and Mini-TES $\tau_{1075,dust}$ (normal-incidence) is quite good. This provides an important degree of validation for the model input parameters including the temperature profile.

[47] 2. The apparent discrepancy between the 825 cm^{-1} water ice optical depths ($\tau_{825,ice}$) is likely to be related to the general difficulty of detecting small amounts of water ice with Mini-TES, although selection effects may also play a role. In other words, $\tau_{825,ice} = 0$ for Mini-TES is not inconsistent with the TES results, due to the weighting of Mini-TES data to lower altitudes (see section 7).

[48] 3. The $\tau_{825,ice}$ values are taken from the retrievals using the *Wolff and Clancy* [2003] dust indices of refraction.

The transparency of the 780–900 cm^{-1} region exacerbates the difference in the altitudes sampled by TES and Mini-TES. Given the sensitivity of this frequency range to particle size effects (see section 5.2.2), we are probably seeing the results of the assumption of a constant r_{eff} with altitude. The presence of water ice in the Mini-TES spectrum would actually minimize this problem, so the null Mini-TES values of $\tau_{825,\text{ice}}$ (as indicated in Table 2 footnote) would tend to support the supposition of particle size effects.

[49] 4. The data for sols 22B and 46A show a clear dominance of the dust component; the IR ice-dust optical depth ratios are very small, $\omega_S = 0.92$, and the best-fit scattering phase function is “Tomasko.” For sol 68B and beyond, one views a distinct trend toward an increasing abundance of water ice, at least with respect to the $\tau_{825,\text{ice}}$ values for TES.

[50] 5. The similarity of the visible-IR extinction ratios (from MER) for sols 22B and 46A, in addition to the consistency of the TES-MER retrievals, strongly suggests the presence of similar atmospheric dust properties.

[51] From Table 2, we identify the observing period to be used in deriving the optical constants and the retrieval algorithm validation for the Mini-TES analyses, and determine the parameters to be used in constraining particle size.

5.2. Dust Indices of Refraction

[52] One must consider two more variables, vertical mixing ratio and particle size, before arriving at the derivation of the IR complex indices of refraction ($m = n + ik$). However, the process of constraining these two removes the remaining ambiguity in the direct determination of m .

5.2.1. Vertical Mixing Ratio

[53] Given the limitation of useful aerosol retrieval sensitivity to the region above an altitude of ~ 20 km (due to large air mass factors in the limb paths below this height), our goal is a limited characterization of the vertical mixing profile for the period near sols 22B and 46A, $L_S = 350^\circ$. In essence, we wish to test for the case where dust might be significantly confined to altitudes below the peak of the Mini-TES aerosol contribution functions (e.g., $\lesssim 20$ km; see also Figure 8). More specifically, we are attempting to discriminate between cases which are fairly well-mixed (i.e., $\nu \sim 0.01$ [Conrath, 1975]) from those which are significantly confined (i.e., $\nu \gtrsim 0.2$). However, given the weak dependence of $\tau_{1075,\text{dust}}$ on the “Conrath” vertical mixing profile, $q(z)$, for perturbations about a given value of ν (section 4.4), we anticipate that a high degree of precision will not be required in determining the vertical profile.

[54] We analyze three TES solarband limb sequences using the 3D monte carlo radiative transfer code of Whitney and collaborators [Whitney *et al.*, 1999; Clancy *et al.*, 2003a] and the aerosol properties derived by Clancy *et al.* [2003b]. We determine q_0 by adopting the TES retrievals of $\tau_{1075,\text{dust}}$ for the nadir data of the same region; we require the integral of the column (which includes $q(z)$) to equal $\tau_{1075,\text{dust}}$, using q_0 effectively as a normalization constant. For Spirit, we use the TES data that bracket the rover site in the north-south direction: OCK 23744 ($L_S = 350^\circ$) where the limb tangent points are near (180°W , 24°S), and OCK 23857 ($L_S = 354^\circ$) near (182°W , 4°N). For Opportunity, we examine a single profile near the site: OCK 23675 ($L_S =$

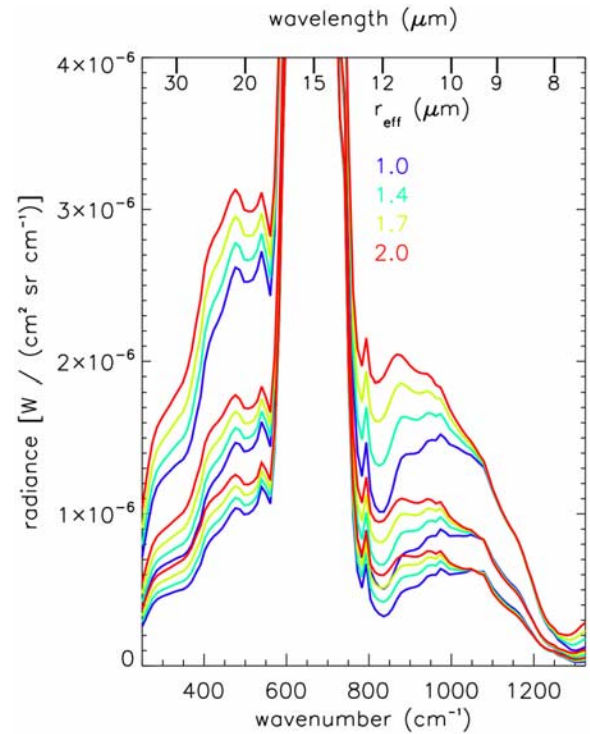


Figure 12. The effect of r_{eff} on Mini-TES radiances for elevation angles of 10° , 20° , and 30° . With the exception of r_{eff} , the model parameters are the same as those for Figure 4. The regions of sensitivity, 350–550 cm^{-1} and 800–950 cm^{-1} , are similar to those for ν_{eff} , as is the lack thereof in the 1050–1200 cm^{-1} range.

347°) near (6°W , 4°S). The Spirit profiles are consistent with $\nu \sim 0.00$ – 0.01 (i.e., well-mixed to ~ 35 – 40 km) for the northern point to ~ 0.01 – 0.03 (i.e., well-mixed to ~ 25 km) at the southern point. The data near Opportunity appear similar to the southern profile for Spirit in that the derived $q(z)$ is represented by a ν value in the 0.01–0.03 range. Both of those locations also appear to possess a detached cloud layer above 35 km, corresponding to the water vapor condensation level for the TES limb-derived $T(p)$ and the expected water vapor abundance of 5–10 $\text{pr-}\mu\text{m}$ [Smith, 2002; Smith *et al.*, 2006]. Given that the water ice optical depths in the monte carlo solar band analyses of ~ 0.01 – 0.03 , there is essentially no impact of such water ice clouds at >35 km on the Mini-TES spectra.

[55] Considering the above results and the Mini-TES contribution functions, we adopt $\nu = 0.01$ for the $L_S = 350^\circ$ epoch. This value allows for the presence of smaller particles at higher altitudes while remaining in approximate agreement with the monte carlo analyses. In other words, the lower cross sections of smaller particles would require an increased number density to produce the same radiance as that by larger particles; the net result is a more well-mixed vertical profile than that for $\nu \sim 0.03$ case (assuming fixed particle size). Unless otherwise indicated, we use this value ($\nu = 0.01$) for all retrievals presented in this paper.

5.2.2. Particle Sizes

[56] Particle size represents the proverbial “last, but not least” parameter. As illustrated in Figure 12, for a fixed $\tau_{1075,\text{dust}}$, r_{eff} can have a significant effect on Mini-TES

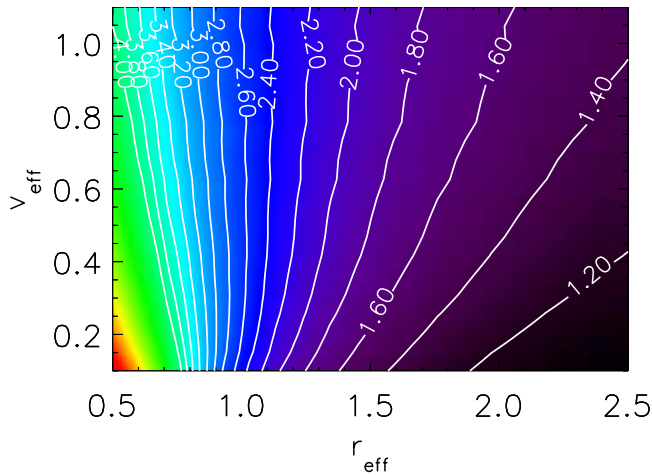


Figure 13. Visible-to-IR optical depth ratio for a $k(1075 \text{ cm}^{-1}) = 0.70$ model. The image is a map of the extinction cross section ratio of $0.88 \mu\text{m}$ to 1075 cm^{-1} . We calculate the cross sections using a gamma distribution [e.g., Hansen and Travis, 1974], spherical particles, m_{IR} from Wolff and Clancy [2003], and $m_{0.88}$ from Tomasko et al. [1999]. Given the importance in the accuracy of $m_{0.88}$, we note that the adopted values are in very good agreement with the recent analysis of Pancam data by Lemmon et al. [2004].

model spectra. Although not shown, a similar trend for v_{eff} exists as one moves to increasing values, the amplitude of the differences are appreciably smaller for the range of plausible values ($v_{eff} = 0.2\text{--}0.8$ [cf., Clancy et al., 2003b]). Clearly, the ranges $350\text{--}550 \text{ cm}^{-1}$ and $800\text{--}950 \text{ cm}^{-1}$ offer a significant constraint for determining the dust size distribution for a given m . At the same time, the importance in adequately determining r_{eff} and, to a lesser extent, v_{eff} in the process of obtaining a new set of m values cannot be underestimated. Fortunately, by combining the results of the coordinated overflight campaign with previous Pathfinder and Pancam analyses, one can place appreciable constraints on the size distribution.

[57] The visible-IR optical depth ratio is a powerful diagnostic, and one whose components can be accurately obtained from MER data. We use this ratio because the amount of opacity needed to reproduce a particular 1075 cm^{-1} radiance is fairly model-independent. The degree of dependency is related to the relative importance of scattering at 1075 cm^{-1} . While this is certainly greater for the Mini-TES geometry than for that of TES (e.g., Figure 4), Figure 12 shows a reasonably small sensitivity to r_{eff} for the adopted m at 1075 cm^{-1} , particularly when compared to the $400\text{--}500 \text{ cm}^{-1}$ region. When combined with prior knowledge of refractive indices at the relevant visible wavelength(s) (here $0.88 \mu\text{m}$), the visible-IR ratio and its associated precision trace the region in the $r_{eff} - v_{eff}$ plane for a given value of m at 1075 cm^{-1} . One can see this in Figures 13 and 14, where we use the $m_{visible}$ from Pathfinder and Pancam analyses [Tomasko et al., 1999; Lemmon et al., 2004] and two different IR “compositions” ($k = \text{Im}(m)$ values at 1075 cm^{-1}). In the figures, a given ratio value defines distinct regions in the $r_{eff} - v_{eff}$ plane. The two cases considered are chosen to illustrate composi-

tional “end-member” extremes: palagonite-like and montmorillonite-like materials [e.g., Toon et al., 1977; Clancy et al., 1995; Hansen, 2003]. Fortunately, the imposition of additional size constraints, particularly those on r_{eff} , can potentially validate or eliminate the viability of a specific composition. In addition, such information can usefully decrease the area of the plausible $r_{eff} - v_{eff}$ region.

[58] Using Pancam “sky survey” data from observations taken during our “dusty epoch,” Lemmon et al. [2004] derive a dust size of $r_{eff} = 1.5 \pm 0.2 \mu\text{m}$. Their assumption of $v_{eff} = 0.2$ is based upon earlier Pathfinder analyses, and should be considered a lower limit [Tomasko et al., 1999]. For sol 22B and 46A, we have $\tau_{0.88}/\tau_{1075,dust} = 2.2 \pm 0.04$. However, treating the particles as spheres may introduce up to $\sim 10\%$ uncertainty into the $0.88 \mu\text{m}$ (Pancam filter) extinction cross section, so we expand the overall uncertainty range in the ratio to ± 0.25 . Applying both constraints to the map of Figure 13, we find $r_{eff} \simeq 1.3\text{--}1.5 \mu\text{m}$ with $v_{eff} \lesssim 0.25$. We begin with $r_{eff} = 1.4 \mu\text{m}$ and $v_{eff} = 0.6$, where the latter is chosen (somewhat arbitrarily) to be on the “large” end of the plausible range [e.g., Wolff and Clancy, 2003]. However, we wish to note that the use of the $k(1075 \mu\text{m}) = 0.7$ map as a starting point is somewhat arbitrary. Starting with size distribution values for any $k(1075 \mu\text{m})$ values for which the above restrictions are not mutually exclusive, result in essentially the same m . In other words, we cannot start with the $k(1075 \mu\text{m}) = 1.25$ case, since there is no region in the map which satisfies the observed Vis-IR ratio and the Pancam/Pathfinder size constraints.

5.2.3. Derivation

[59] The actual process of deriving a set of optical constants contains another iterative process, as well as an interactive evaluation of the goodness-of-fit as applied to all of the data sets. Although we initially considered a single elevation scan each from two sols, we ultimately expanded the data set to a total of seven sequences, all within 30 minutes of the highest elevation angle of the overflight: 2 from sol 29A, 1 from sol 22B, 2 from sol 46A, 1 from sol 54A, and 1 from sol 55A. The bias toward Spirit data originates with the larger systematic calibration effects in

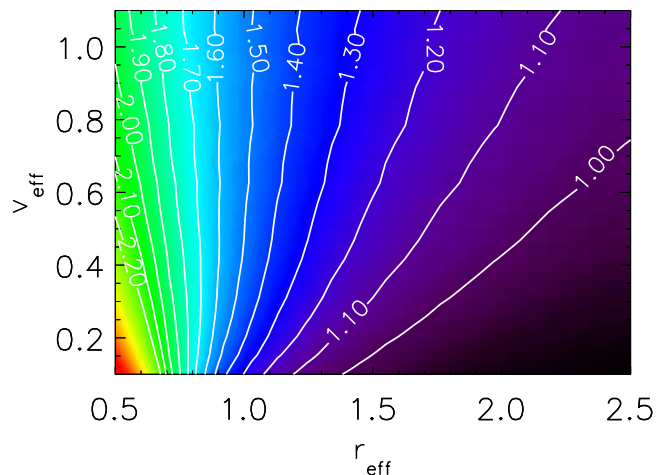


Figure 14. Visible-to-IR optical depth ratio for a $k(1075 \text{ cm}^{-1}) = 1.25$ model. As for Figure 13, except that we take m_{IR} from Hansen [2003].

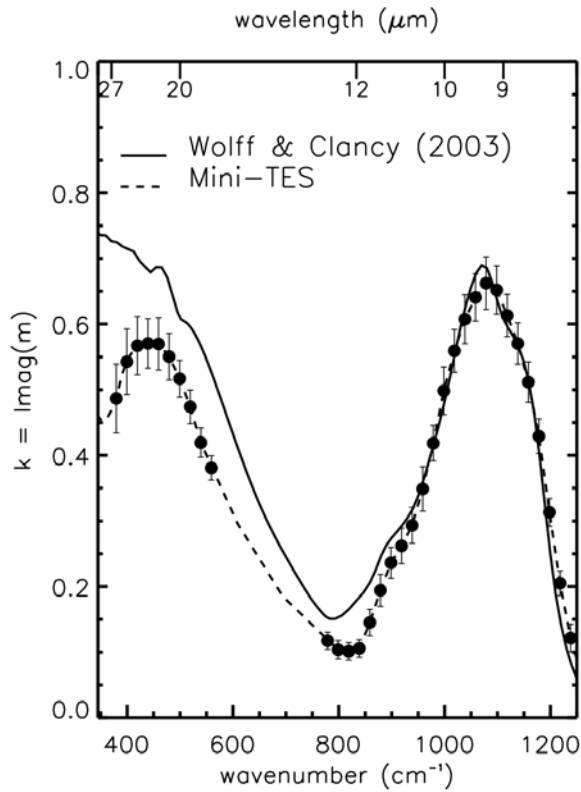


Figure 15. Derived imaginary indices of refraction (dashed line, $k = \text{Im}(m)$) compared with the starting values (solid line) from *Wolff and Clancy* [2003]. The filled circles indicate the position of each Mini-TES channel. We compute the error bars using the averaged formal retrieval precision and the standard deviation among the k values from all seven data sets, added in quadrature assuming no correlation.

the Opportunity data and the uncertainty related to the correction [e.g., *Smith et al.*, 2006]. We treat each data set independently, applying the following steps:

[60] 1. Assume $m = n + ik$; either an “initial guess” or the result of the previous iteration.

[61] 2. Using only data from 1050–1300 cm^{-1} , retrieve $\tau_{1075,dust}$ and T_{surf} , where the latter is allowed to vary by ± 5 K around the value determined from the surface Mini-TES data (as described in section 4.2).

[62] 3. A repeat of the previous step, but for data in the 780–1300 cm^{-1} range and bounding T_{surf} by ± 5 K with respect to that just obtained. This step is empirically motivated and provides improved convergence properties for our algorithm. Numerically, the 1050–1300 cm^{-1} region has reduced sensitivity of the to many of the radiative transfer inputs.

[63] 4. For each channel in the 380–560 cm^{-1} and 780–1300 cm^{-1} intervals, we retrieve only k , i.e., all other parameters have been fixed.

[64] 5. From the new k , we get n from a subtractive Kramers-Kronig [cf. *Snook*, 1999], using $n(0.5 \mu\text{m}) = 1.5$ as the fixed point [*Tomasko et al.*, 1999].

[65] The sequence of five steps is typically run six times, by which point the relative change in k (and n) has dropped

below the 1% level for most of the spectral range. That is to say, in each case, we explicitly demand and test for the occurrence such convergence in m . Next, we average the m from each of the seven data sets, and use the resulting average to perform retrievals on the seven data sets as well as on the TES spectra from the 22B and 46A campaigns. For Mini-TES, we allow r_{eff} to vary and require a consistent value from all seven data sets, and good fits to both TES and Mini-TES observations. We adjust r_{eff} and v_{eff} manually. The “final” Mini-TES size distribution is described by $r_{eff} = 1.4 \mu\text{m}$ and $v_{eff} = 0.3$, where the latter value is primarily a balance between the MER and MGS data in the 800–950 cm^{-1} transparency region. We allow the TES retrieval process to choose the best-fitting r_{eff} , resulting in values in the 1.7–1.9 μm range with an uncertainty of $\sim 0.3 \mu\text{m}$. For the data sets after sol 46A, the small size of $\tau_{1075,dust}$ leads to uncertainties at the 0.5 μm level in r_{eff} [see also *Wolff and Clancy*, 2003]. The discrepancy between the Mini-TES and TES r_{eff} suggests that one might be seeing different particle sizes. However, within the framework of r_{eff} constant with height, we attempt to “split the difference” and avoid unrealistically high $\tau_{825,ice}$ in the TES retrievals while preserving a reasonable fit to the Mini-TES data.

[66] The end-product of this process (i.e., the final iteration) is shown in Figures 15 and 16. The error bars represent the averaged formal retrieval uncertainty (of the last iteration) and the standard deviations of m from the sample of all seven m , added in quadrature under the assumption of no

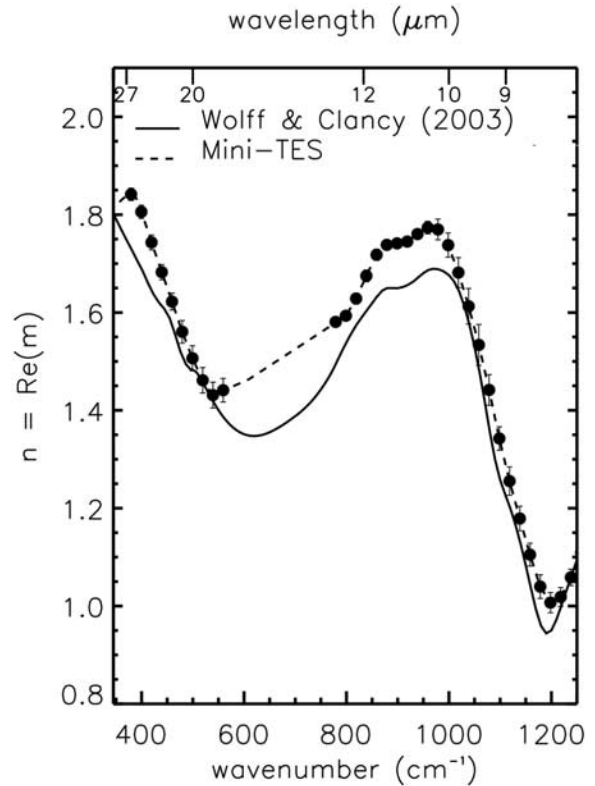


Figure 16. As for Figure 15, but for the real part (n) of the complex indices of refraction. In addition, the error bars represent only the standard deviation from the seven sets of n .

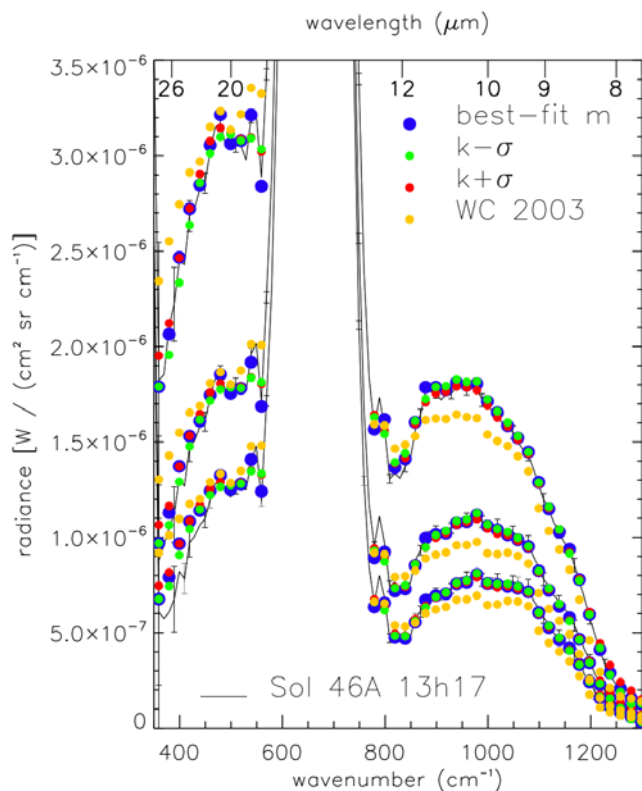


Figure 17. A Mini-TES elevation scan obtained on Sol 46A at 13:17 LTST is compared to several model-fits which represent different indices of refraction: the best-fit m (blue circles), the best-fit k perturbed by $\pm\sigma$ (red and green circles, respectively), and the m from *Wolff and Clancy* [2003] (orange circles, “WC 2003”). The data and errors are treated in the manner described for Figure 1. The first 3 cases give essentially the same $\tau_{1075,dust}$ (0.37) and r_{eff} (1.4 μm), while the WC-based retrieval produces 0.31 and 1.5 μm , respectively. For clarity, the models are generated for a reduced frequency mesh (i.e., every other data point).

correlation between the terms. Figure 17 provides an example of the best-fit m (blue circles) applied to a sol 46A elevation scan. For comparison, we also include the cases where k has been perturbed by the $1 - \sigma$ uncertainty (red and green circles for $\pm\sigma$, respectively), as well as the case of the *Wolff and Clancy* [2003] indices of refraction (orange circles). The reduced χ^2 for the best-fit case is ~ 1 , which increases to ~ 2 for the $\pm\sigma$ fits to the data (as would be expected if the errors are adequately represented [e.g., *Bevington and Robinson*, 1992]) and to ~ 12 for the *Wolff and Clancy* [2003] case. Ultimately, it is clear that the updated m provide a significantly improved fit to the Mini-TES data as compared to a set of indices derived only from orbitally based data.

6. Application to Mini-TES

[67] Having the new refractive indices in hand, several applications to a larger sample size (of Mini-TES data) quickly present themselves: *normal-incidence* dust optical depths, dust effective particles sizes, and vertical mixing. As discussed by *Smith et al.* [2006], the presence of dust on the

Mini-TES optics eventually becomes an issue in terms of a “contamination” of the atmospheric radiance. While they provide a prescription for removing this effect, there is a non-trivial degree of uncertainty introduced by such a correction. We prefer to avoid the issue of such uncertainty and its potential bias on our analyses by concentrating on data from the periods before such a correction is required: sols 1 to 400 for Spirit and 1 to 200 for Opportunity. Thus we carry out two sets of retrievals for each sample. The first case fixes the dust vertical profile with $\nu = 0.01$, consistent with our analyses of TES solarband limb data for the sol 22B,46A epoch. The second series allows ν to be a free parameter.

6.1. Dust Optical Depths

[68] For the defined range of sols, we show the 1075 cm^{-1} normal-incidence extinction optical depth for Spirit and Opportunity in Figures 18 and 19, respectively. In order to identify potential systematic time-of-day effects (e.g.,

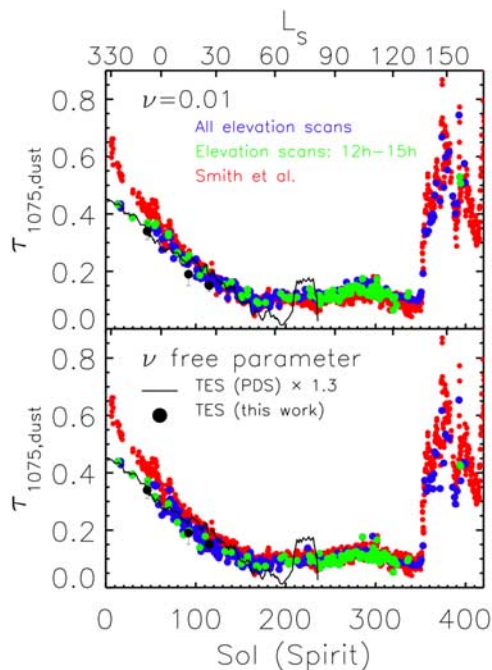


Figure 18. The 1075 cm^{-1} dust (normal-incidence) optical depth observed by Spirit through sol 400 (top) for $\nu = 0.01$ and (bottom) for ν as a free parameter. For the range shown, one typically finds the errors in $\tau_{1075,dust}$ to be $\simeq 0.02 - 0.03$. We distinguish between the elevation scans in and out of the MGS-block by color. We include the Mini-TES retrievals performed with an independent approach by *Smith et al.* [2006] (red circles). For comparison, the TES overflight values are shown from the three coordinated campaigns (black filled circles) as well as from all MGS (black line) blocks, where the latter is taken from the Planetary Data System ATM-files and scaled by 1.3 (to account for the translation from absorption to extinction [e.g., *Clancy et al.*, 2003b]). The TES IR spectrometer was turned off due to instrumental concerns in August 2004. The strange behavior of the plotted TES retrievals in the month (or so) prior to turnoff raise the question of whether some “issues” with the instrument occurred sooner. The PDS data are smoothed with a boxcar filter using a 5-sol width.

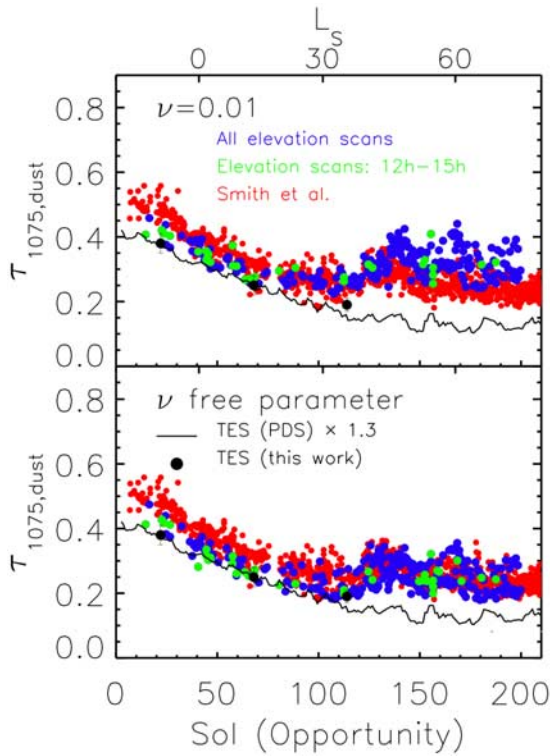


Figure 19. As for Figure 18, but using Opportunity data through sol 200. One sees a systematic discrepancy between this work and that of *Smith et al.* [2006] near sol 140. Curiously, this is near an inflection point in the Instrumental Response Function temporal correction. However, it may also be the point at which the dust on the optics is becoming statistically significant; we are not accounting for that effect in our work.

retrieval-related biases such as $T(p)$, we chose a different color for the results from the broad MGS-block (green versus blue points). Our results are compared with the empirical approach employed by *Smith et al.* [2006] (red points), as well as with $\tau_{1075,dust}$ for the associated TES overflights. The TES values include those for the three coordinated overflights for each rover (black points) and those from the Planetary Data Systems (PDS) archive (i.e., the “ATM” files [cf., *Smith et al.*, 2000]) for each overflight (black line). The PDS data are scaled by 1.3 to account for the conversion of $\tau_{absorption}$ to $\tau_{extinction}$ [e.g., *Clancy et al.*, 2003b]. The upper and lower panels represent the two cases for the ν : fixed- and free-parameters. However, it is important to note that *only our Mini-TES retrievals change between the two panels*. The error associated with $\tau_{1075,dust}$ (from Mini-TES) is estimated to be the largest of the following: (0.02 for Spirit, 0.03 for Opportunity), 5% of the retrieved value, and the formal parameter uncertainty (i.e., the diagonal terms of the covariance matrix). Because the formal precision of $\tau_{1075,dust}$ can exceed 10% during the lower opacity season (near aphelion), the error value is typically $\simeq 0.02$ – 0.03 ; similar to, if not somewhat smaller than, that found by *Smith et al.* [2006].

[69] *Smith et al.* [2006] discuss the seasonal trends associated with $\tau_{1075,dust}$. Here, we concentrate on the similarities and differences between the $\tau_{1075,dust}$ values

from the different sources (i.e., Mini-TES, TES, empirical versus our work), as well as the effects on $\tau_{1075,dust}$ when allowing ν to vary. As discussed previously in section 4.4, increasing ν generally decreases the upward-viewing retrieved $\tau_{1075,dust}$ while increasing that for TES. Nevertheless, several clear trends exist for both cases, although the degree to which they hold is somewhat dependent on the vertical mixing profile treatment:

[70] 1. While there is some indication that the observations in the MGS-block possess less scatter, the consequences of using the TES $T(p)$ for morning and evening observation in retrieving of $\tau_{1075,dust}$ appear to be less dire than for the extreme cases in our sensitivity experiment.

[71] 2. For $\tau_{1075,dust} \lesssim 0.35$ – 0.4 , there is good agreement between the two Mini-TES analysis methods (i.e., empirical (red) versus refractive index (blue and green)), at least for similar vertical mixing profiles: uniform mixing versus $\nu = 0.01$. Above this level, one sees a systematic departure with increasing optical depth, possibly due to the increasing amount of scattering and limitations inherent in the two-stream algorithm employed by *Smith et al.* [2006]. One also sees a divergence between the results of the two after sol 140 on Opportunity. This is likely to be related to the effects of dust on the optics becoming statistically significant, earlier than we had hoped. The fact that the ν -free case agrees well here is suspect, given the assumption of well-mixed dust by *Smith et al.* [2006].

[72] 3. The relationship between the Mini-TES (blue and green circles) and the PDS TES (black line) values remains close for the early part of the mission. However, by about sol 170A ($L_S \simeq 50^\circ$) and 110B ($L_S \simeq 35^\circ$, earlier for $\nu = 0.01$), the agreement begins to breakdown. The scale factor seems reasonable, given the good agreement between the value from the PDS and our coordinated overflights. However, the scaling factor of 1.3 is a representative value that does tend to break down at low dust optical depths near the equator at aphelion [*Wolff and Clancy*, 2003]. The aphelion cloud belt forms earlier at Opportunity’s latitude than at Spirit’s [*Clancy et al.*, 1996; *Wolff et al.*, 1999]. Thus the earlier divergence between TES and Mini-TES at Opportunity is consistent with the inapplicability of a single scale factor. As an aside, the sudden rise for TES near sol 210 may be related to the instrumental issues that ultimately resulted in a power-off approximately one month later.

6.2. Particle Sizes

[73] Figures 20 and 21 illustrate the observed trends in r_{eff} ($\nu_{eff} = 0.3$) throughout our sample of the Mini-TES observations. Because we derive our refractive indices with $r_{eff} = 1.4 \mu\text{m}$, it is not surprising that both rovers find this size at the times corresponding to those overflights. Allowing for systematic effects, as calculated in part by the rms, we estimate the precision to be in the range 0.1 – $0.2 \mu\text{m}$. ν does not greatly affect the retrievals, though the ν -free case appears to have a higher degree of scatter. With these uncertainties and caveats in mind, one can identify clear trends in r_{eff} that are distinctly different, though modest, for each rover. In general, changes in r_{eff} accompany those in the other retrieved parameters, but they appear to be robust. The r_{eff} trend at Spirit increases in a serpentine fashion from $1.4 \mu\text{m}$ to a peak of about $\sim 1.6 \mu\text{m}$ near sol 280, which corresponds to a local maximum in $\tau_{1075,dust}$. The subse-

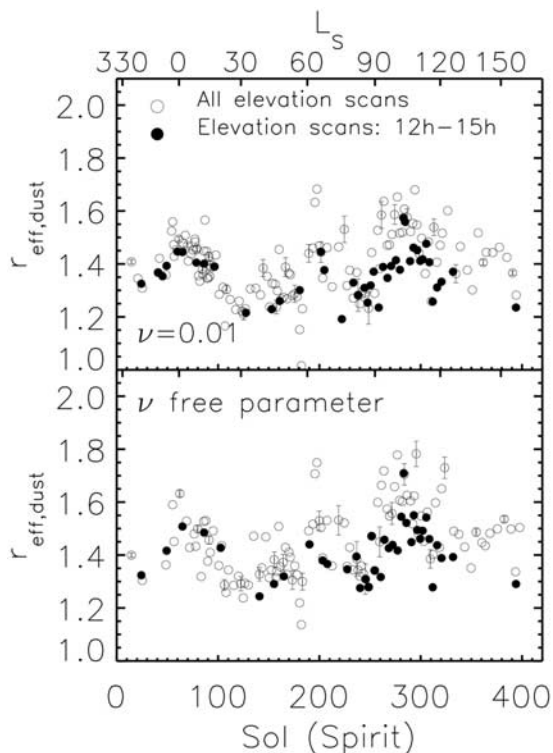


Figure 20. Values of r_{eff} for dust from Spirit Mini-TES data through sol 400 (top) for $\nu = 0.01$ and (bottom) for ν as a free parameter. We fix the second moment of the size distribution (ν_{eff}) at 0.3 from the analyses in section 5.2. For clarity, the original retrievals are binned using a 3-point width, and every fifth error bar is shown. The error bars represent the formal precision of the retrieval that can appreciably underestimate the scatter in the data. We estimate the effective precision on r_{eff} to be $\pm 0.1\text{--}0.2 \mu\text{m}$. For r_{eff} , the effect of ν does not seem particularly dramatic.

quent decrease in size does end abruptly with the onset of the local dust storm activity after sol 350, though the change in size is not dramatic within the errors. For Opportunity, there is a quasi-linear trend from $1.4 \mu\text{m}$ to $1.7 \mu\text{m}$ at sol 140. At this point, a clear decline occurs (modest but with seemingly small scatter) that correlates with the trend in $\tau_{1075,\text{dust}}$, followed again by an increase.

6.3. Dust Vertical Distribution

[74] Figures 22 and 23 provide the ν values that were retrieved simultaneously with those in the bottom panels of Figures 18–21. Both rovers show the same tantalizing trend: a reasonably monotonic increase from well-mixed vertical profiles near the beginning of landed operations to significantly confined by $L_S \sim 30^\circ$. Of additional interest is the distinct drop and subsequent rise (well outside of the large retrieval uncertainties and apparent rms scatter) that correspond well to the onset of regional dust activity near Spirit around sols 340–350. We adopted the “Conrath parameterization” (section 4.4) of the vertical mixing profile with the primary goal of adequately representing the dust distribution above the $\sim 15 \text{ km}$ level. That functional form for $q(z)$ with its single term (as opposed to a series of weighted exponential terms) does not handle particularly well the presence of the additional components that one

might anticipate in the bottom scale-height or planetary boundary layer such as increased mixing ratios near the surface. As a result, we choose to bound the value of ν to be ≤ 1 (see Figure 11). The lack of error bars in the figure at this boundary are an artifact of MPFIT constraint process. The accuracy of large ν values is somewhat suspect, perhaps reflecting an aliasing process for an additional (time-variable), more confined dust component. Nevertheless, the trends between confined and well-mixed dust appear robust. Furthermore, the behavior appears to correlate with the initial onset of the colder aphelion climate (the descent of the water vapor saturation point (a.k.a. hygro-pause) with the colder temperatures and increasing water vapor columns) and of the dust storm activity. Future work may benefit from the potentially greater sensitivity to vertical effects in the higher vertical resolution manifested in new Mini-TES sequences (added near the end of the first Mars year of operations) and from the more extensive use TES limb data.

7. Discussion

7.1. Indices of Refraction

[75] The derivation of m presented here possesses a distinct advantage over previous efforts [e.g., Toon *et al.*, 1977; Clancy *et al.*, 1995; Snook, 1999; Wolff and Clancy, 2003; Hansen, 2003] by dint of the contemporaneous MGS-MER visible and IR observations. We are able leverage the increased of the data sensitivity to m (through the sensitivity of Mini-TES to the scattering component, as opposed to using only orbital data) and to place significant constraints on the several input parameters. However, our results are

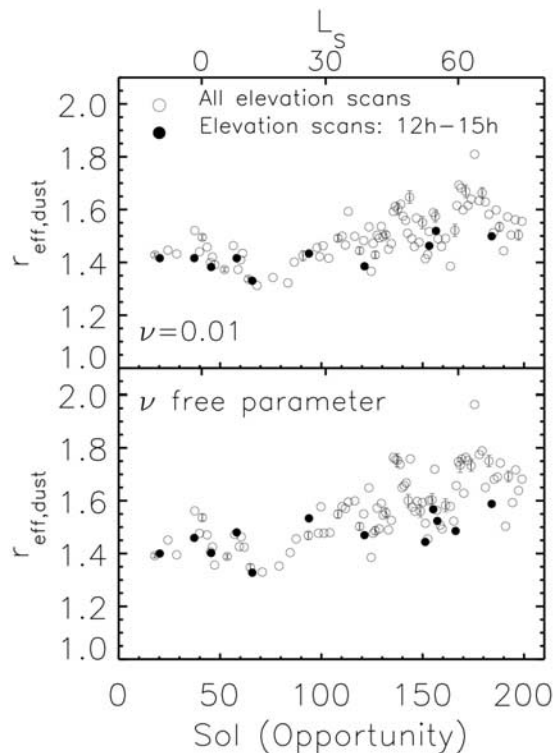


Figure 21. As for Figure 20, but using Opportunity data through sol 200. Allowing ν to be a free parameter increases the scatter among the retrievals, while preserving the general trend.

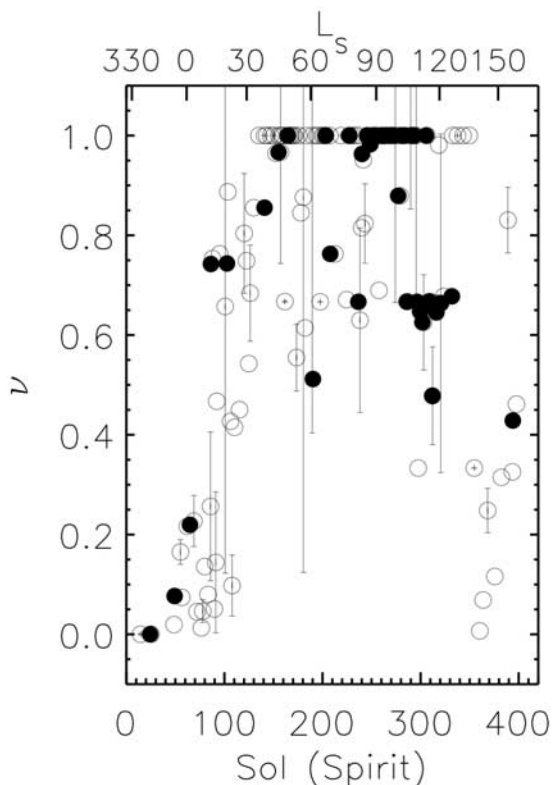


Figure 22. The ν parameter of our dust vertical profile parameterization [Conrath, 1975] from Spirit Mini-TES data through sol 400. The symbols are the same as those in Figure 20, though every third error bar is displayed. We do not allow ν to exceed unity. When the parameter reaches this, it will possess a formal precision of zero if it retains the value of 1 at convergence; this is an artifact of the constraint process. That is to say, the algorithm wants to increase ν in order to improve the fit as indicated by the Jacobian matrix. The attempt to do so resets the “guess” to 1, with the resulting precision of 0 simply reflecting the absence of change in the new model during the unsuccessful attempt to exceed $\nu = 1$.

not without potential weak-points. In particular, we refer to the adopted value of m for the Pancam 0.88 μm -band cross sections. Combining $m_{0.88}$ with the related Pancam results for r_{eff} , we eliminate a large amount of the degeneracy related to particle size and to the total number of particles in the column (a.k.a. the value of k at 1075 cm^{-1} [cf. Hansen, 2003]). In addition, we assume a size distribution that does not vary with altitude. We felt that the height-independent approach was the most robust, introducing the fewest assumptions and minimized the sources of uncertainty in deriving m . However, previous work does indicate the presence of a gradient [e.g., Chassefière et al., 1995]. We will visit briefly the subject of a size gradient and its potential impact on retrievals in a subsequent section.

[76] Subject to the above caveats, it is not unreasonable to consider that the utility of our indices of refraction has been demonstrated, at least with respect to Mini-TES and to a frequency range subset for TES. They produce consistent results across a wider temporal span of observational conditions than used in their derivation, as well as provides a

noticeable improvement in fit quality for TES in the 380–500 cm^{-1} range as compared to the m of Wolff and Clancy [2003]. Although not shown, we also find agreement with respect to the alternate retrieval approach of Smith et al. [2006]. The frequency dependence of their extinction efficiency and single scattering albedo values is quite consistent with those produced here with $r_{\text{eff}} = 1.4 \mu\text{m}$ and $\nu_{\text{eff}} = 0.3$.

[77] A final aspect we wish to touch upon is that of dust aerosol composition. Among previous investigations into this subject, some consider the question of composition in order to provide the indices of refraction appropriate to Martian aerosols through the use of terrestrial analogs [e.g., Toon et al. [1977]; Clancy et al., 1995, and references therein]. Others start with m and calculate an emissivity spectrum with the goal of deconvolving the associated mineralogy [e.g., Hamilton et al., 2005]. At the risk of stating the obvious, both of these approaches may find some additional leverage through our results. Even without invoking the optical regime, the synthesis of Mini-TES and TES places limits on the general classes of carriers for the 500 and 1075 cm^{-1} dust features: k values outside an acceptable range cannot account for the contributions of both absorption and scattering. Even with the reported uncertainty in m , it seems reasonable that one could produce synthetic emissivity spectra with these m values for particle sizes relevant to various spectral libraries.

7.2. Water Ice Clouds

[78] We have not reported specific water ice optical depths for Mini-TES because the values for our samples appear to be essentially zero, within the uncertainties. This is despite the fact the water ice effects occur in the

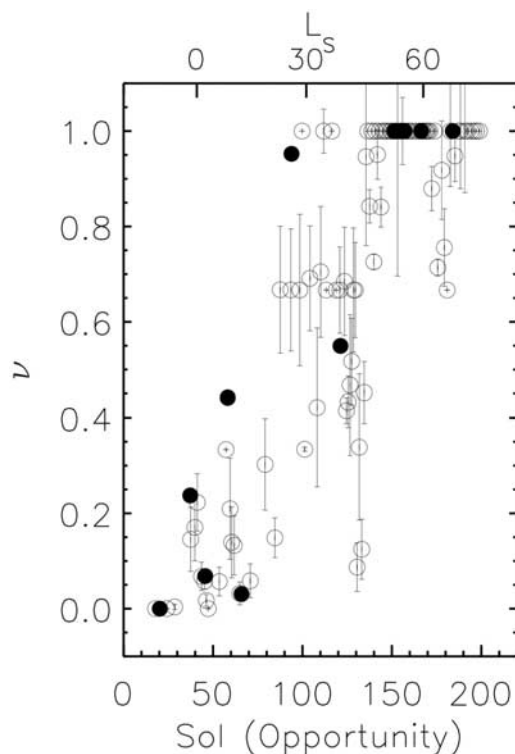


Figure 23. As for Figure 22, but using Opportunity data through sol 200.

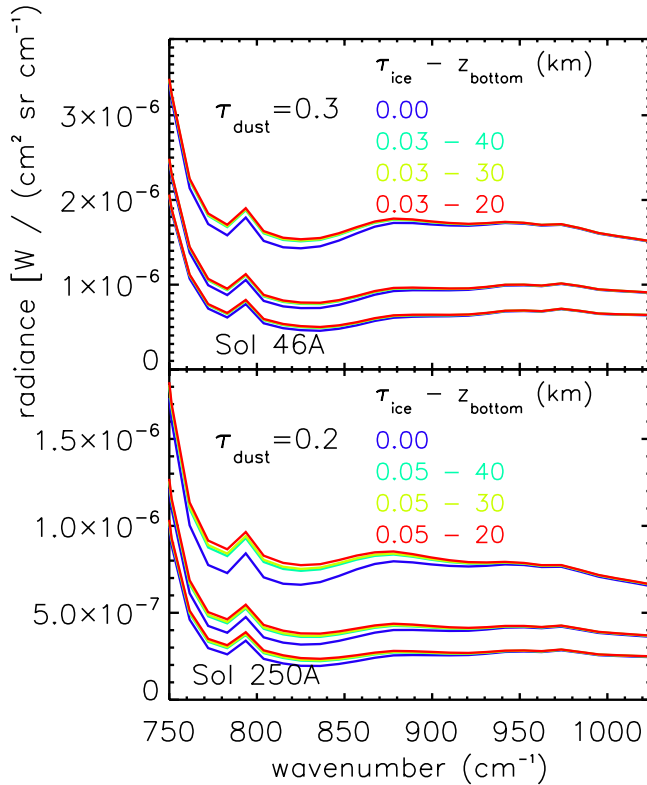


Figure 24. Effect of water ice on Mini-TES radiances for (top) typical equinox and (bottom) solstice conditions. Model radiances are computed for elevation angles of 10° , 20° , and 30° (from highest radiances to lowest). We represent equinox with $T(p)$ from sol 46A, $T_{surf} = 270$ K, and $\tau_{1075,dust} = 0.3$ and solstice with $T(p)$ from 250A, $T_{surf} = 250$ K, and $\tau_{1075,dust} = 0.15$. In both cases, we adopt “Type 1” ice ($r_{eff} = 2 \mu\text{m}$, $v_{eff} = 0.1$). The color coding indicates the height at which the cloud layer begins; dust is distributed vertically using $\nu = 0.01$.

transparency region between the dust and CO_2 features. While this may seem counterintuitive given the rover observing geometry, we illustrate the crux of the problem in Figure 24. Early in landed operations, when radiance rms errors are small due to a warm atmosphere, one expects very little water ice [Smith, 2004]. Conversely, during the aphelion cloud belt period ($L_S \sim 80\text{--}140^\circ$ [Wolff et al., 1999; Clancy et al., 2003b; Smith, 2004]), the rms errors are large. For the solstice (sol 250A) case shown in the bottom panel, the errors are on the order of 10% in the region of the ice feature. Even the seasonal descent of the water vapor saturation height to the 10–20 km range near the solstice does not provide increase in sensitivity to water ice clouds (see Figure 24). At the same time, the presence of a more confined dust column (as suggested by our results) will decrease the detectability. Finally, one must contend with additional specter of systematic calibration effects for Opportunity and the level of uncertainty associated with correction [Smith et al., 2006]. Clearly, the unambiguous identification of water ice clouds from Mini-TES is a more difficult proposition than one would hope.

[79] The latitude of Spirit lies on the southernmost edge of the aphelion cloud belt while that of Opportunity is closer to the center. Both the TES results from the coordinated campaigns and general TES climatology [Smith, 2004] indicate the presence of water ice clouds at or near the rover sites through this season. Yet, through $L_S = 180^\circ$ of the first year of operations, no clouds have been identified in any of the imaging data for Spirit, and only a small number detections are known for Opportunity [Wolff et al., 2005]. The correlation of these facts raises several questions. Are undetected clouds present and, if so, are we suffering from insufficient sampling? Do clouds often possess an extremely diffuse nature? Are there local or regional meteorological effects at the rover locations that inhibit water ice cloud formation? Do the orbital results reflect an average over thick discrete clouds with a low areal filling factor over the rover sites? At this point, there is some evidence to suggest that it is likely a combination of several of these, e.g., MOC imaging (B. Cantor and M. Malin, personal communications, 2005). These topics will be explored in a subsequent paper which will focus specifically on water ice clouds at and near the rover sites, including Mini-TES beyond the range of sols considered here.

7.3. Particle Size (Vertical) Gradients

[80] The sol 22B-46A overflight results of $r_{eff} = 1.4 \mu\text{m}$ and $1.7\text{--}1.9 \mu\text{m}$ for Mini-TES and TES, respectively, hint at the presence of a vertical gradient in particle sizes. While the precision of these values is such that one could declare them consistent, we would like to explore, albeit briefly, the ramifications of considering r_{eff} to be a function of altitude.

[81] To begin, we perform a simple numerical experiment. We generate a set of synthetic spectra for $\tau_{1075,dust} = 0.3$ using our m and the vertical distribution of r_{eff} given by Chassefière et al. [1995]. In their prescription for a fixed v_{eff} , r_{eff} goes from $2.0 \mu\text{m}$ to $1.7 \mu\text{m}$ to $1.0 \mu\text{m}$ at 0 km, 10 km, and 25 km (and above) in altitude, respectively; 0–10 km altitude range is an extrapolation on their part. The vertical mixing profile is again our old favorite, $\nu = 0.01$. We find that the synthetic elevation scan is best fit by $r_{eff} \simeq 1.7 \mu\text{m}$ and $\tau_{1075,dust} = 0.33$, while we retrieve $r_{eff} \simeq 1.9 \mu\text{m}$ and $\tau_{1075,dust} = 0.27$ from the TES nadir simulation. These results give the flavor of the systematic effects involved. Recalling the contribution functions from Figure 8 and allowing for the non-scattering assumption in their generation, our experiment confirms what we have intuitively assumed. Mini-TES aerosol retrievals probe higher altitudes than do those of TES. The resulting mismatch in the two $\tau_{1075,dust}$ values stems from the implicit incompatibility of using the same m for mutually exclusive assumptions: $r_{eff}(z)$ versus $r_{eff} = \text{constant}$.

[82] Next, we perform a small permutation on the previous experiment. We produce a set of radiances for Mini-TES and TES using $r_{eff} = 1.4 \mu\text{m}$ and $1.8 \mu\text{m}$ respectively ($v_{eff} = 0.3$). In other words, this exercise is attempting to find a non-constant distribution that is consistent with the two different sizes. Applying a minimalist approach, we iterate on the 0 km and 10 km altitude points in the Chassefière et al. [1995] distribution. Even with this degree of simplicity, the character of phase space has changed such that we resort to interactive fitting (e.g., *chi-by-eye*). Ultimately, we arrive

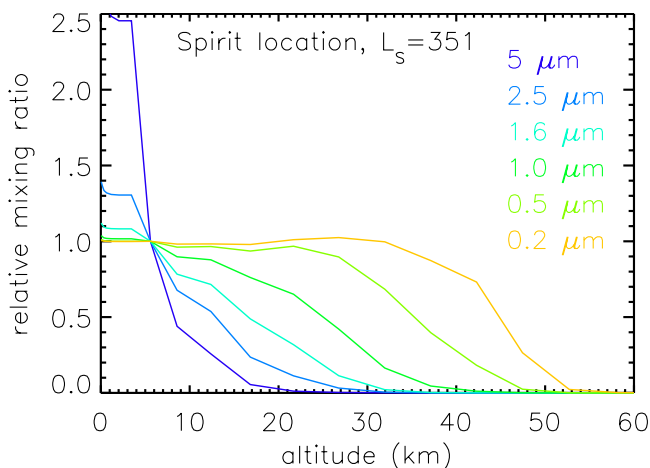


Figure 25. Mars GCM simulation of the vertical mixing profile for 6 representative particle sizes. The grid cell location is the Spirit site at 14:00 for $L_S = 351^\circ$. For convenience, the profiles have been normalized to an altitude of ~ 6 km. Each profile can be scaled to construct the desired size distribution at any height, thus giving the size distribution at all heights.

at ($r_{eff} =$) $1.7 \mu\text{m}$ and $1.3 \mu\text{m}$ for 0 km and 10 km; with $\tau_{1075,dust} = 0.28$. The quality of the fit is reasonable and provides a consistent optical depth for both orbital and surface “observations.”

[83] A final observational suggestion of particle size gradient may be seen in the potential correlation of r_{eff} and ν seen in Figures 20–23: r_{eff} seems to increase with ν . This would be consistent with “seeing larger particles” as a result of the altitude decrease in the contributions functions with increasing ν ; putting more dust closer to the surface will lower the regions probed by Mini-TES in both the non-scattering and multiple-scattering approaches. We hope to be able to investigate this further in the future using the higher resolution elevation scans obtained more recently.

[84] We performed numerous additional experiments similar to those detailed above. Unfortunately, the primary conclusion appears to be that it is difficult to generalize about the effects of a particle size gradient on Mini-TES and TES spectra. Nevertheless, this is a situation that can be guided by additional data, both observational and numerical. Solar and stellar occultations observations, such as those being performed by the SPICAM instrument on Mars Express, allow for the separation of mixing ratio and particle size effects [Bertaux et al., 2005]. In addition, the combination of optical and multi-wavelength IR limb observations offer a similar capability, though at the cost of a significant computational intensity and retrieval complexity. Finally, one needs to consider the use of global circulation models (GCMs). In particular, the tracer transport schemes can provide vertical profiles for particles of different sizes as a function of location, local time, and season. Figure 25 shows an example from the Mars GCM of R. J. Wilson et al. (personal communication, 2006) [see also Hinson and Wilson, 2004; Basu et al., 2004]. Because each size is handled discretely, one can scale the mixing profiles to provide the desired size distribution at a particular height,

giving the size at all heights. The utility of this product includes parameterization studies (i.e., developing a functional form suitable for retrieval algorithms), interpolation and extrapolation schemes, as well as null-hypothesis testing (e.g., is the vertical profile of r_{eff} consistent with observations?).

8. Summary

[85] The coordinated contemporaneous overflight campaigns between MGS and the two MER rovers offer a unique opportunity to better constrain the properties of Martian dust aerosols, beginning with one of the most fundamental: the indices of refraction. Because the upward-viewing geometry of Mini-TES is significantly more sensitive to scattering by dust than is the equivalent IR observation from orbit, atmospheric retrievals can place significant constraints on both n and k (i.e., $m = n + ik$). Of course, deriving m in this manner while maintaining a reasonable level of uncertainty requires determining values for the menagerie of other radiative transfer input parameters.

[86] Using the data from six coordinate overflight campaigns, which occurred during the first four months of landed MER operations, we identified a subset of observations ($L_S \simeq 350^\circ$) that appear to be appropriate for the derivation of dust refractive indices. We then carried out a series of radiative transfer analyses for the Mini-TES and the TES (solarband and IR spectrometer) data sets, providing the initial constraints for the determination of m . By combining these results with literature values for $m_{visible}$ and an independent estimate of particle size from the rovers for the same epoch, we derived the indices of refraction for the $380\text{--}1300 \text{ cm}^{-1}$ range (excluding the 667 cm^{-1} CO_2 band).

[87] Subsequently, we applied the new m to a much larger sample of Mini-TES data, but restricted our sample set in order to minimize the potential impact of systematic effects in the Mini-TES calibration. We noted the following aspects in our retrievals of $\tau_{1075,dust}$, r_{eff} , and ν (optical depth, effective radius, and vertical mixing profile parameter):

[88] 1. The error associated with $\tau_{1075,dust}$ is estimated to be the maximum of (0.02 for Spirit, 0.03 for Opportunity), 5% of the retrieved value, and the formal retrieval uncertainty. This produces typical error values of $\simeq 0.02\text{--}0.03$ for the sample analyzed.

[89] 2. Comparisons of $\tau_{1075,dust}$ and radiative properties (frequency dependence of optical depth and single scattering albedo) with the empirical approach of Smith et al. [2006] show generally good agreement for similar assumptions.

[90] 3. $\tau_{1075,dust}$ for Mini-TES and TES agree well until about sols 170A and 110B, at which point systematic effects in the PDS TES values related to the use of a single scale factor (to convert absorption to extinction) may cause disagreement.

[91] 4. r_{eff} varies between about $1.2 \mu\text{m}$ and $1.6 \mu\text{m}$ for Spirit, and $1.4 \mu\text{m}$ and $1.8 \mu\text{m}$ for Opportunity. Changes in the trends typically correlate with those in $\tau_{1075,dust}$, particularly for Spirit. The error associated with r_{eff} is estimated to be $\simeq 0.1\text{--}0.2 \mu\text{m}$.

[92] 5. For the “Conrath” mixing parameter, ν , both rovers reveal a reasonably monotonic increase from well-

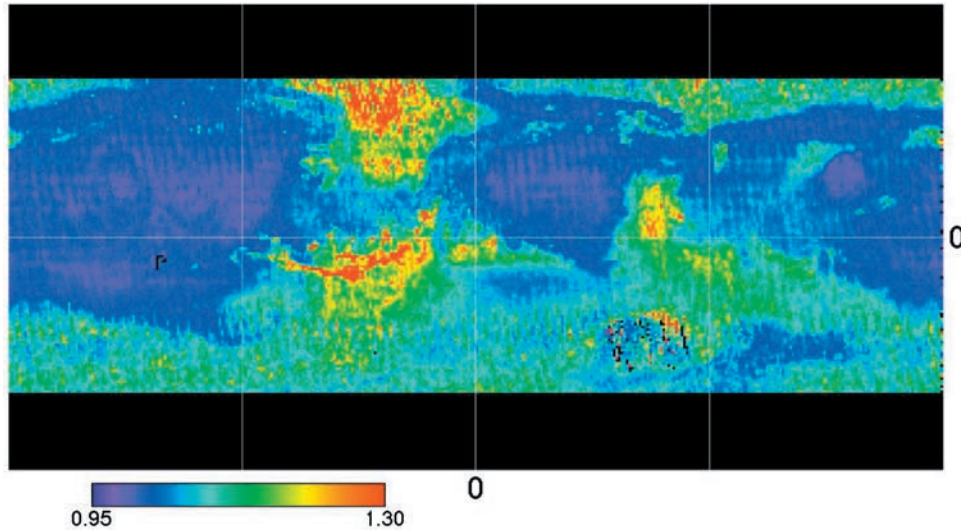


Figure A1. The ratio of a map generated from the TES standard solarband Lambert albedo to that of one from our atmospherically corrected version of the Lambert albedo. The data are map-projected and resampled in $1^\circ \times 1^\circ$ bins from 60°S to 60°N . Eastern longitude runs to the right, with the $\pm 90^\circ$ longitudes also indicated. The color bar quantifies the value of the ratio. Values less than unity reflect the effect of dust on very bright areas, while the larger values represent atmospheric effects of dark regions.

mixed vertical profiles near the beginning of landed operations to significantly confined dust mixing by $L_S \sim 30^\circ$. For Spirit, there is a distinct drop and subsequent rise that correspond to the onset of regional dust activity.

[93] Additional discussion and results were provided for the topics of the refractive indices, the lack of definitive detection of water ice clouds in Mini-TES observations, and the presence of vertical gradients in particle size distribution. Of final note, we presented an atmospheric-correction scheme for the TES solarband Lambert albedo and briefly illustrated its effects.

Appendix A: Corrected Solarband Lambert Albedo

[94] We derive surface Lambert albedo values, where the effects of the atmosphere have been removed, through a combined process of data filtering and radiative transfer models. We select TES data from the beginning of mapping through orbit $\sim 20,000$ for which the incidence angles are less than 80° , the emergence angles are less than 20° , and IR absorptive optical depths (i.e., those delivered to the Planetary Data System in the “ATM” files) are less than 0.25 and 0.15 for dust and water ice aerosols, respectively. We perform the transformation of the solarband radiance-on-sensor to a “true” Lambert albedo with a six-dimensional cube (incidence angle, emergence angle, azimuth angle, Lambert albedo, dust optical depth, ice optical depth) of ~ 70 million radiative transfer models. For an observation, we use the five known parameter values and the nearest-neighbor algorithm (for computational efficiency) to generate a Lambert albedo spectrum as a function of radiance-on-sensor, and then employ a cubic-spline algorithm to derive the specific Lambert albedo. We minimize the errors associated with the nearest-neighbor approach (as compared with an interpolation scheme) by tessellating the

input grid for the six-dimensional cube based upon the value ranges found in the input data set itself. We run the DISORT-based radiative transfer code with 32 streams and solarband-specific aerosol properties of *Clancy et al.* [2003b]. We assume that the dust is uniformly mixed from the surface upward, while the water ice particles are uniformly mixed starting at an altitude of 25 km. Furthermore, we consider the case of only Type 1 ice (e.g., $r_{\text{eff}} \sim 2 \mu\text{m}$ [see *Clancy et al.*, 2003b]).

[95] We illustrate the amplitude of the atmospheric correction on a global scale in Figure A1, which we generate from the ratio of a map of TES Lambert albedo to that of corrected albedo. For the uncorrected data, we require $\tau_{1075,\text{dust}} \leq 0.3$ and $\tau_{825,\text{ice}} \leq 0.10$. While one can certainly be more restrictive with the atmospheric conditions, our goal is to include as much of the data as possible while maintaining an acceptable level of error in the correction. To give a sense of the absolute numbers, we provide a few examples. On the side of greatest change in albedo, $\sim 30\%$, we find a value in Mellas Chasma (pixel 46.5°W , 13.5°N) that changes from 0.13 to 0.10, while in northern Acidalia Planitia (pixel 34.5°W , 45.5°N) the change is from 0.12 to 0.083. More moderate changes, the 10–20% level, are found in Syrtis Major and south of Valles Marineris. These results compare well with the aerosol effects on the surface albedo as determined from Viking solarband EPF analyses [*Clancy and Lee*, 1991]. Thus the need of the atmospheric correction depends upon the region of interest. As discussed previously (section 3.3), the EPF analyses did benefit from the corrected Lambert albedo values.

[96] **Acknowledgments.** We wish to acknowledge and thank the entire MER science and operations team. Undoubtedly, our analyses would have not been possible without their constant effort. We also thank the TES and Mini-TES teams for providing for observation sequences that executed simultaneously; in many cases, Mini-TES was observing literally while

MGS was through its field of view. We have benefited also from the time and assistance of R. John Wilson. We wish to thank Karly Pitman for her amazingly thorough review of this manuscript as well as to acknowledge the helpful comments of an anonymous reviewer (including his/her prompting about the correlation between r_{eff} and ν). This work was funded by NASA through the Mars Exploration Rover Project, a portion of which was carried out at the Jet Propulsion Laboratory, California Institute of Technology, under a contract with the National Aeronautics and Space Administration.

References

- Arvidson, R. E., J. Bibring, F. Poulet, S. W. Squyres, M. Wolff, and R. Morris (2004), Coordinated Mars Exploration Rover and Mars Express OMEGA observations over Meridiani Planum, *Eos Trans. AGU*, 85(47), Fall Meet. Suppl., Abstract P24A-06.
- Arvidson, R. E., F. Poulet, J.-P. Bibring, M. Wolff, A. Gendrin, R. V. Morris, J. J. Freeman, Y. Langevin, N. Mangold, and G. Bellucci (2005), Spectral reflectance and morphologic correlations in Eastern Terra Meridinae, Mars, *Science*, 307, 1591–1594.
- Bandfield, J. L. (2002), Global mineral distributions on Mars, *J. Geophys. Res.*, 107(E6), 5042, doi:10.1029/2001JE001510.
- Bandfield, J. L., and M. D. Smith (2003), Multiple emission angle surface-atmosphere separations of Thermal Emission Spectrometer, *Icarus*, 161(1), 47–65, doi:10.1016/S0019-1035(02)00025-8.
- Bandfield, J. L., P. R. Christensen, and M. D. Smith (2000), Spectral data set factor analysis and end-member recovery: Application to analysis of Martian atmospheric particulates, *J. Geophys. Res.*, 105(E4), 9573–9588.
- Basu, S., M. I. Richardson, and R. J. Wilson (2004), Simulation of the Martian dust cycle with the GFDL Mars GCM, *J. Geophys. Res.*, 109, E11006, doi:10.1029/2004JE002243.
- Bell, J. F., III, et al. (2003), Mars Exploration Rover Athena Panoramic Camera (Pancam) investigation, *J. Geophys. Res.*, 108(E12), 8063, doi:10.1029/2003JE002070.
- Bell, J. F., III, J. Joseph, J. N. Sohl-Dickstein, H. M. Arneson, M. J. Johnson, M. T. Lemmon, and D. Savransky (2006), In-flight calibration and performance of the Mars Exploration Rover Panoramic Camera (Pancam) instruments, *J. Geophys. Res.*, 111, E02S03, doi:10.1029/2005JE002444.
- Bertaux, J.-L., et al. (2005), Global structure and composition of the Martian atmosphere with SPICAM on Mars Express, *Adv. Space Res.*, 35, 31–36.
- Bevington, P. R., and D. K. Robinson (1992), *Data Reduction and Error Analysis for the Physical Sciences*, 2nd ed., McGraw-Hill, New York.
- Chassefière, E., P. Drossart, and O. Korabiev (1995), Post-Phobos model for the altitude and size distribution of dust in the low Martian atmosphere, *J. Geophys. Res.*, 100(E3), 5525–5539.
- Christensen, P. R., et al. (2001), Mars Global Surveyor Thermal Emission Spectrometer experiment: Investigation description and surface science results, *J. Geophys. Res.*, 106(E10), 23,823–23,872.
- Christensen, P. R., et al. (2003), Miniature Thermal Emission Spectrometer for the Mars Exploration Rovers, *J. Geophys. Res.*, 108(E12), 8064, doi:10.1029/2003JE002117.
- Christensen, P. R., et al. (2004a), Initial results from the Mini-TES Experiment in Gusev Crater from the Spirit Rover, *Science*, 305, 837–842.
- Christensen, P. R., et al. (2004b), Mineralogy at Meridiani Planum from the Mini-TES Experiment on the Opportunity Rover, *Science*, 306, 1733–1739.
- Clancy, R. T., and S. W. Lee (1991), A new look at dust and clouds in the Mars atmosphere: Analysis of emission-phase-function sequences from global Viking IRTM observations, *Icarus*, 93, 135–158.
- Clancy, R. T., S. W. Lee, G. R. Gladstone, W. W. McMillan, and T. Roush (1995), A new model for Mars atmospheric dust based upon analysis of ultraviolet through infrared observations from Mariner 9, Viking, and Phobos, *J. Geophys. Res.*, 100, 5251–5264.
- Clancy, R. T., A. W. Grossman, M. J. Wolff, P. B. James, D. J. Rudy, Y. N. Billawala, B. J. Sandor, S. W. Lee, and D. O. Muhleman (1996), Water vapor saturation at low altitudes around aphelion: A key to Mars climate?, *Icarus*, 122, 36–62.
- Clancy, R. T., M. J. Wolff, B. A. Whitney, and B. A. Cantor (2003a), Vertical distributions of dust optical depth during the 2001 planet encircling storm from a spherical radiative transfer analysis of MOC limb images, in *Sixth International Conference on Mars*, Abstract 3205, Lunar and Planet. Inst., Houston, Tex.
- Clancy, R. T., M. J. Wolff, and P. R. Christensen (2003b), Mars aerosol studies with the MGS TES emission phase function observations: Optical depths, particle sizes, and ice cloud types versus latitude and solar longitude, *J. Geophys. Res.*, 108(E9), 5098, doi:10.1029/2003JE002058.
- Conrath, B. J. (1975), Thermal structure of the Martian atmosphere during the dissipation of the dust storm of 1971, *Icarus*, 24, 36–46.
- Conrath, B. J., J. C. Pearl, M. D. Smith, W. C. Maguire, P. R. Christensen, S. Dason, and M. S. Kaelberer (2000), Mars Global Surveyor Thermal Emission Spectrometer (TES) observations: Atmospheric temperatures during aerobraking and science phasing, *J. Geophys. Res.*, 105, 9509–9520.
- Gladstone, G. R., J. W. Kaminski, R. Link, and J. C. McConnell (1984), Cloud radiance modeling: Phase II, *Contract KMI47-4-1041*, Can. Dep. of the Environ., Ottawa, Ontario, Canada.
- Hamilton, V. E., H. Y. McSween Jr., and B. Hapke (2005), Mineralogy of Martian atmospheric dust inferred from thermal infrared spectra of aerosols, *J. Geophys. Res.*, 110, E12006, doi:10.1029/2005JE002501.
- Hanel, R. A., B. J. Conrath, D. E. Jennings, and R. E. Samuelson (2003), *Exploration of the Solar System by Infrared Remote Sensing*, 2nd ed., Cambridge Univ. Press, New York.
- Hansen, G. B. (2003), Infrared optical constants of Martian dust derived from Martian spectra, in *Sixth International Conference on Mars*, Abstract 3194, Lunar and Planet. Inst., Houston, Tex.
- Hansen, J. E., and L. D. Travis (1974), Light scattering in planetary atmospheres, *Space Sci. Rev.*, 16, 527–610.
- Hinson, D. P., and R. J. Wilson (2004), Temperature inversions, thermal tides, and water ice clouds in the Martian tropics, *J. Geophys. Res.*, 109, E01002, doi:10.1029/2003JE002129.
- Hunt, G. E. (1979), On the opacity of Martian dust storms by Viking IRTM spectral measurements, *J. Geophys. Res.*, 84, 8301–8310.
- Kieffer, H. H., T. Z. Martin, S. C. Chase Jr., E. D. Miner, F. D. Palluconi, G. Muench, and G. Neugebauer (1976), Infrared thermal mapping of the Martian surface and atmosphere—First results, *Science*, 193, 780–786.
- Lemmon, M. T., et al. (2004), Atmospheric imaging results from the Mars Exploration Rovers: Spirit and Opportunity, *Science*, 306, 1753–1756.
- Martin, T. Z. (1986), Thermal infrared opacity of the Mars atmosphere, *Icarus*, 66, 2–21.
- Moré, J. J., D. C. Sorensen, K. E. Hillstrom, and B. S. Garbow (1984), The MINPACK Project, in *Sources and Development of Mathematical Software*, edited by W. J. Cowell, Prentice-Hall, Upper Saddle River, N. J.
- Ockert-Bell, M. E., J. F. Bell III, J. B. Pollack, C. P. McKay, and F. Forget (1997), Absorption and scattering properties of the Martian dust in the solar wavelengths, *J. Geophys. Res.*, 102(E4), 9039–9050.
- Pitman, K. M., J. L. Bandfield, and M. J. Wolff (2006), MGS-TES phase effects and thermal infrared directional emissivity field measurements of Martian analog sites, *Proc. Lunar Planet. Sci. Conf. 37th*, Abstract 1336.
- Smith, M. D. (2002), The annual cycle of water vapor on Mars as observed by the Thermal Emission Spectrometer, *J. Geophys. Res.*, 107(E11), 5115, doi:10.1029/2001JE001522.
- Smith, M. D. (2004), Interannual variability in TES atmospheric observations of Mars during 1999–2003, *Icarus*, 167, 148–165.
- Smith, M. D., J. L. Bandfield, and P. R. Christensen (2000), Separation of atmospheric and surface spectral features in Mars Global Surveyor Thermal Emission Spectrometer (TES) spectra, *J. Geophys. Res.*, 105(E4), 9589–9608.
- Smith, M. D., et al. (2004), First atmospheric science results from the Mars Exploration Rovers Mini-TES, *Science*, 306, 1750–1752.
- Smith, M. D., M. J. Wolff, N. Spanovich, A. Ghosh, D. Banfield, P. R. Christensen, G. A. Landis, and S. W. Squyres (2006), One Martian year of atmospheric observations using MER Mini-TES, *J. Geophys. Res.*, 111, E12S13, doi:10.1029/2006JE002770.
- Snook, K. J. (1999), Optical properties and radiative heating effects of dust suspended in the Mars atmosphere, Ph.D. thesis, Stanford Univ., Stanford, Calif.
- Snook, K. J., J. L. Bandfield, F. Forget, and C. P. McKay (2000), Derivation of infrared optical properties of dust suspended in the Martian atmosphere from MGS-TES data, *Bull. Am. Astron. Soc.*, 32, 51.08.
- Stamnes, K., S. C. Tsay, W. Wiscombe, and K. Jayaweera (1988), Numerically stable algorithm for discrete ordinate method radiative transfer in multiple scattering and emitting layered media, *Appl. Opt.*, 27, 2502–2509.
- Thomas, G. E., and K. Stamnes (1999), *Radiative Transfer in the Atmosphere and Ocean*, 517 pp., Cambridge Univ. Press, New York.
- Tomasko, M. G., L. R. Dooze, M. Lemmon, P. H. Smith, and E. Wegryn (1999), Properties of dust in the Martian atmosphere from the Imager on Mars Pathfinder, *J. Geophys. Res.*, 104(E4), 8987–9008.
- Toon, O. B., J. B. Pollack, and C. Sagan (1977), Physical properties of the particles composing the Martian dust storm of 1971, *Icarus*, 30, 663–696.
- Whitney, B. A., M. J. Wolff, and R. T. Clancy (1999), Monte Carlo radiative transfer models for Mars, in *Fifth International Conference on Mars*, Abstract 6213, Lunar and Planet. Inst., Houston, Tex.
- Wolff, M. J., and R. T. Clancy (2003), Constraints on the size of Martian aerosols from Thermal Emission Spectrometer observations, *J. Geophys. Res.*, 108(E9), 5097, doi:10.1029/2003JE002057.

- Wolff, M. J., et al. (1999), Hubble Space Telescope observations of the Martian aphelion cloud belt prior to the Pathfinder mission: Seasonal and interannual variations, *J. Geophys. Res.*, 104(E4), 9027–9042.
- Wolff, M. J., R. T. Clancy, K. M. Pitman, J. F. Bell, and P. B. James (2001), Constraints on Martian aerosol particles using MGS/TES and HST data: Shapes, *Eos Trans. AGU*, 82(47), Fall Meet. Suppl., Abstract P32E-05.
- Wolff, M. J., R. T. Clancy, D. Banfield, and K. Cuzzo (2005), Water ice clouds as seen from the Mars Exploration Rovers, *Eos Trans. AGU*, 86(52), Fall Meet. Suppl., Abstract P21E-02.
-
- J. L. Bandfield and P. R. Christensen, Department of Geological Sciences, Arizona State University, Tempe, AZ 85287, USA.
- D. Banfield, J. F. Bell III, and S. W. Squyres, Department of Astronomy, Cornell University, 428 Space Sciences Building, Ithaca, NY 14853, USA.
- R. T. Clancy, B. A. Whitney, and M. J. Wolff, Space Science Institute, 4750 Walnut Street, Suite 205, UCB 564, Boulder, CO 80301, USA. (wolff@spacescience.org)
- A. Ghosh, Tharsis Inc., Gaithersburg, MD, USA.
- G. Landis, NASA Glenn Research Center, Cleveland, OH 44135, USA.
- M. T. Lemmon, Department of Atmospheric Sciences, Texas A&M University, College Station, TX 77843, USA.
- M. D. Smith, NASA Goddard Space Flight Center, Code 693, Greenbelt, MD 20771, USA.
- N. Spanovich, Jet Propulsion Laboratory, Pasadena, CA 91125, USA.